Digital Comprehensive Summaries of Uppsala Dissertations
from the Faculty of Science and Technology 2505

Mesoscopic and Atomistic Insights into the Microstructural Evolution of Energy Storage Materials

SOUZAN HAMMADI

ACTA UNIVERSITATIS
UPSALIENSIS
2025

ISSN 1651-6214
ISBN 978-91-513-2388-6
urn:nbn:se:uu:diva-550510

UPPSALA
UNIVERSITET

Dissertation presented at Uppsala University to be publicly examined in Lecture hall Sonja Lyttkens, Ångströmlaboratoriet, Lägerhyddsvägen 1, Uppsala, Friday, 4 April 2025 at 09:15 for the degree of Doctor of Philosophy. The examination will be conducted in English. Faculty examiner: Professor Arnulf Latz (University of Ulm).

Abstract

Hammadi, S. 2025. Mesoscopic and Atomistic Insights into the Microstructural Evolution of Energy Storage Materials. *Digital Comprehensive Summaries of Uppsala Dissertations from the Faculty of Science and Technology* 2505. 63 pp. Uppsala: Acta Universitatis Upsaliensis. ISBN 978-91-513-2388-6.

Energy storage is possible through the incorporation of Li-electron pairs into battery electrodes. Depending on the nature of the interactions between the species within electrode materials, different atomic arrangements can form. Weak interactions result in an even distribution of Li forming a solid solution phase, while strong interactions result in short range order and ultimately in phase separation. A material that undergoes phase separation during battery operation is $LiFePO_4$ and structural mismatch at the Li-rich (LFP) and Li-poor (FP) phase boundaries create strain fields that, over time, lead to mechanical damage. This material showcases both phase separation and solid solution behaviour at different conditions due to its complex short and long range order at the atomic scale. Understanding the factors underlying Li order is, therefore, important to avoid unwanted aging effects and in the design of more efficient electrode materials. This is explored in this thesis using computational modelling at many scales.

A phase-field model is developed to evaluate the effect of the charge transfer rate on the microstructural evolution at the mesoscale. Two models of charge transfer are confronted, the Butler-Volmer model of ion transfer and the Marcus-Hush-Chidsey model of electron transfer. Depending on the model and the chosen input, different discharge rates and microstructures can be expected. The microstructure evolution also depends on the free energy landscape which generally is approximated with the regular solution model. In contrast, many free energy descriptions parameterized on experimental data showcase an asymmetric form with a third local minima. This minimum represents a metastable solid solution that evolves at room temperature when integrated into the phase-field model.

Such an asymmetric energy landscape is also to be expected as the short range order of LFP is lower than in FP. This indicates that accessing the solid solution phase is easier during Li extraction. Addition of dopants such as Mn further decreases the short range order in the material. Finding routes to stabilize the solid solution phase in LFP will ultimately enhance the battery cycling rate and mechanical stability as seen in the phase-field model, where higher rates and lower strains are now possible.

Keywords: materials chemistry, computational modelling, energy storage

Souzan Hammadi, Department of Chemistry - Ångström, Structural Chemistry, Box 538, Uppsala University, SE-751 21 Uppsala, Sweden.

ISSN 1651-6214
ISBN 978-91-513-2388-6
URN urn:nbn:se:uu:diva-550510 (http://urn.kb.se/resolve?urn=urn:nbn:se:uu:diva-550510)

Tillägnad mina föräldrar, Montaha och Muwaffak

List of papers

This thesis is based on the following papers, which are referred to in the text by their Roman numerals.

I **Hammadi, S.**, Broqvist P., Brandell D., Ofori-Opoku N. Investigation of charge transfer models on the evolution of phases in lithium ion phosphate batteries using phase-field simulations. Journal of Materials Chemistry A. 13, 2849-2858 (2025).

II **Hammadi, S.**, Ofori-Opoku, N., Brandell, D, Broqvist, P. Consecutive intra-particle phase transitions in $LiFePO_4$ battery electrodes. *In manuscript.*

III **Hammadi, S.**, Kullgren, J., Wolf, M. J., Brandell, D., Broqvist, P. Impact of temperature on short-range charge ordering in $LiFePO_4/FePO_4$. Physical Review B, 109(14), 144103 (2024).

IV **Hammadi, S.**, Schwarz, F., Kullgren, J., Brandell, D, Broqvist, P. Cluster analysis of Mn-doped $LiFePO_4$. *In manuscript.*

Reprints were made with permission from the publishers.

Contents

1 Introduction 1
1.1 Rechargeable batteries 1
1.1.1 Electrode materials 2
1.1.2 The $LiFePO_4$ system 3
1.2 Modelling at many scales 6
1.3 Scope of the thesis 8

2 Thermodynamics of solids 9

3 Methodology 16
3.1 Modelling the meso scale 16
3.2 Modelling the atomic scale 21
3.2.1 Statistically sampling the energy landscape 22
3.2.2 Predicting energies by clusters 23
3.2.3 Density Functional Theory 25
3.2.4 Controlling ionic and electronic degrees of freedom 28

4 Phase transitions in $LiFePO_4$ 29
4.1 Microstructural evolution 29
4.1.1 Charge transfer kinetics 30
4.1.2 Impact of the free energy landscape 34
4.2 Ordering at the atomic scale 40
4.2.1 Fitting an interaction model 40
4.2.2 Coordination between Li-Li and Li-Fe(II) 43
4.2.3 The effect of doping 45

5 Conclusions and future work 49

6 Acknowledgement 52

7 Populärvetenskaplig sammanfattning 54

References 57

List of symbols

LFP	$LiFePO_4$
FP	$FePO_4$
SS	solid solution
F	Helmholtz free energy but also the energy functional in phase-field
Ω	regular solution coefficient
c	concentration
E	Young's modulus
ν	Poisson's ratio
M	mobility
D	diffusion coefficient
μ	chemical potential
f_{chem}	chemical free energy
f_{elast}	elastic energy
f_{grad}	gradient energy
ε	eigenstrain
C	stiffness matrix
σ	strain
κ	gradient energy coefficient
J	charge transfer rate
FEM	Finite Element Modelling
BV	Butler-Volmer
MHC	Marcus-Hush-Chidsey
j_0	exchange current density
η	overpotential
V_m	molar volume
$\Delta\Phi$	applied potential
λ	reorganizational energy
k	rate constant
L	interface width
acc($1\rightarrow 2$)	acceptance probability of a move from state 1 to state 2
DFT	Density Functional Theory
+ U	Hubbard correction
OMC	Occupation Matrix Control
CALPHAD	CALculation of PHase Diagrams

1. Introduction

As we combat climate change, the efficient storage of energy from renewable sources is becoming increasingly critical [1]. Rechargeable batteries have demonstrated good energy storage capabilities and have significantly impacted modern society. Fundamentally, the concept of a rechargeable battery is ingenious in its simplicity: positively charged chemical species move across boundaries, generating an electrical current that powers devices. However, these charged species can encounter various obstacles during their journey, and the boundaries they cross can themselves undergo chemical and mechanical damage [2]. This thesis investigates such encounters from a computational perspective.

1.1 Rechargeable batteries

Most commercial rechargeable batteries today are based on the storage of Li ions. A schematic illustration of such as system is depicted in Figure 1.1.

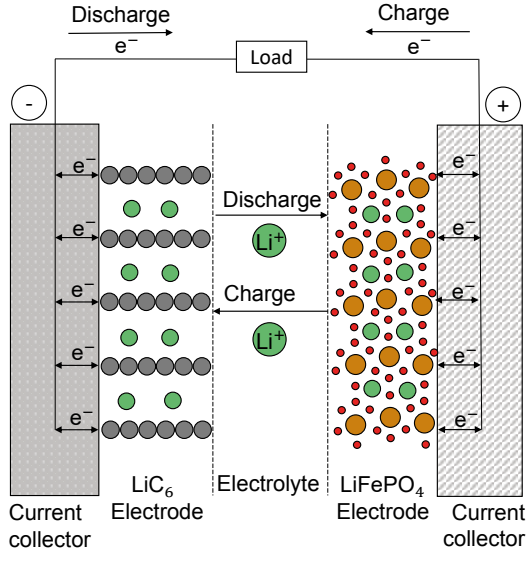

Figure 1.1. Schematics of a rechargeable Li ion battery.

As we discharge such a battery, Li ions move from the negative electrode to the positive electrode though a medium called an electrolyte. At the same time,

electrons are released in the outer circuit. For the $LiFePO_4$ (LFP) electrode, the reaction is as follows.

$$LiFe(II)PO_4 \rightleftharpoons Li^+ + e^- + Fe(III)PO_4 \tag{1.1}$$

Li ions incorporate into the crystal structure of $Fe(III)PO_4$ and electrons reduce Fe(III) into Fe(II). The LFP material acts as a host that accommodates Li-electron pairs and discharging the electrode thus proceeds with the dynamic movement of the Li ions and electrons within its crystal structure.

The reversible process of insertion and extraction of Li ions is essential for a rechargeable battery. In layered intercalation electrodes like graphite, Li ions can be incorporated between the graphite layers, while compounds such as LFP have octahedral sites within their crystal structure that accommodate the ions. The electrochemical properties of an electrode material vary depending on the interaction of the species within its structure. One such property is the (dis)charge rate of the battery, which is a direct consequence of how fast Li ions can be inserted and extracted from the electrode. This in turn determines the magnitude of the electric current.

1.1.1 Electrode materials

To reversibly incorporate Li-electron pairs and store energy within electrode materials, pathways for Li and electron transport must exist. These pathways are affected by interactions between the species within the material which can lead to different arrangements of atoms and phases. The spatial Li concentration might then resemble the schematics presented in Figure 1.2.

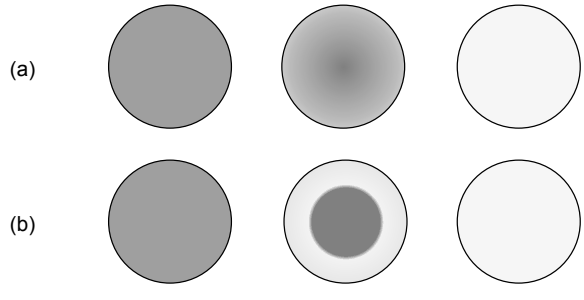

Figure 1.2. Schematics of an electrode particle undergoing delithiation through a) a solid solution and b) phase transition pathway. The spatial Li concentration is given in grey.

When the Li atoms have high solubility within the host structure, they arrange in a disorderd manner creating a so called solid solution phase. This results in a smooth gradient in Li concentration, as shown in Figure 1.2a. In contrast, short range order of Li induces clustering which can eventually result in structural rearrangement and the existence of different phases within

the material. In the latter scenario, the movement of the corresponding phase boundaries, interfaces, span over the long range of entire electrode particles as shown in Figure 1.2b.

This is a very simplified picture of a complicated spatial and temporal rearrangement of atomic species. In reality, there are degrees of short range order and some materials can undergo multiple phase transitions during battery operation [3]. Other electrode materials have thermodynamically stable solid solution phases but still exhibit an interface within the bulk at high battery cycling rates [4].

The presence of such interfaces within the bulk particles affects the mechanical integrity and rate capability of the electrode. Structural mismatch at these boundaries create strain fields that, over time, lead to crack formation and mechanical damage [5]. At the same time, the rate at which Li can be stored and extracted depends on the structural rearrangement as the phases move within the bulk. Consequently, phase changing electrode materials tend to have lower rate capabilities.

Understanding the structural rearrangements in the electrode material is therefore essential in designing durable battery systems with high rate performance. This is one of the reasons for choosing the LFP electrode as a model system in this research study, as it is a material with a high degree of short and long range order that displays both phase transition and solid solution behaviour at different conditions [6, 7].

1.1.2 The $LiFePO_4$ system

Oxides have long played a significant role in battery technology [8]. Many of the first insertion compounds were transition metal oxides in the form of Li_xMO_2 (M = Co, Ni, Mn). Manthiram and Goodenough subsequently identified the polyanion class of electrode materials, which consist of frameworks of XO_4^{n-1}, where X can be elements such as phosphorus (P), silicon (Si) or sulfur (S) [9, 10]. In 1997, Padhi et al. first demonstrated the electrochemical activity of LFP, which naturally occurs as the mineral triphylite [11].

The redox active LFP system has a relatively high theoretical capacity and has a high thermal and structural stability due to its stable PO_4 framework [8]. However, it has a narrow bottleneck as a battery electrode: its electronic conductivity. Work by Armand and coworkers showed that this could be improved by the addition of a conductive carbon layer [12]. This enhanced the charge transfer at the particle surfaces and thereby increased the Li storage capability within the particles. It is thanks to this breakthrough that the LFP electrode is now an alternative to the otherwise more expensive cobalt and nickel containing materials, which are rapidly becoming a global socio-economic issue [13].

Interestingly, while the system has a relatively high capacity for Li, their solubility is quite low. Just like oil separates from water, the LFP system

separates into regions rich in Li (LFP) and regions poor in Li (FP) during battery (dis)charge [14, 15]. The charging of the electrode thus proceeds by the movement of these phases within the material as illustrated in Figure 1.2b. At around 470 K and 60 % Li content, however, a solid solution emerges which is characterized by higher Li disorder [16, 17].

The change in ordering within the crystal structure is a consequence of short and long range interactions between the Li ion and electron pairs. The charge compensating electron is hosted by the Fe(II)/Fe(III) redox couple and the change in oxidation state is accompanied by lattice distortions. This localizes the electrons on specific iron sites, creating so-called small polarons [18]. The polaron is negatively charged and will electrostatically interact with the positively charged Li ion. For every Li position within the structure, there will be several Fe sites for the polaron to occupy.

The mobility of the polarons, Fe(II), increases with Li disorder as the system enters the solid solution phase [19]. This indicates a strong Li-polaron coupling which corresponds well with the calculated high binding energies between these species [20]. However, this does not necessarily mean that the Li and polaron always move as concerted pairs within the structure. Instead, their uncorrelated motion increases with temperature [21] and the configurational entropy of both Li and polarons have to be explored when theoretically reproducing the phase diagram [22]. It is when doing so that the high temperature solid solution phase can be described. This can be summarized as such: at low temperatures, the Li ions and polarons are ordered and the polarons acts as the glue that ties the Li ions together. At high temperatures, the increased activity of the polarons prevents Li ions from clustering. Consequently, the solid solution emerges due to the disorder of Li ions, facilitated by the higher configurational disorder of the polarons [23].

When the LFP electrode was first presented, it was considered a candidate for low rate applications due to its phase changing behaviour at room temperature. In contrast, nanosized particles showcased excellent cycling rates by far surpassing the previously investigated microsized particles. This was explained with a phase-field model that showed how phase transition could be suppressed at high currents resulting in (dis)charge through a solid solution pathway [24, 25]. The presence of a metastable solid solution at high cycling rates was later on experimentally verified [6].

When particles undergo (dis)charge via a solid solution pathway, it impacts the battery in various ways. The absence of an interface reduces strain within the particles and enables (dis)charging at higher rates. Consequently, the phenomenon of possibly accessing a metastable solid solution phase initiated several studies on transport mechanisms in LFP. The previously mentioned phase-field model could reproduce the transition from a two phase to a solid solution at high charging rates by introducing a depth-averaging approximation [24, 25]. This concerns the mode of Li transport, and different types are presented in Figure 1.3.

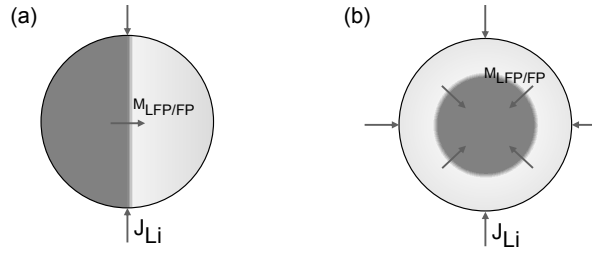

Figure 1.3. Different modes of Li insertion and transport, a) surface insertion and b) bulk mass transport limited growth. The direction of the Li flux is denoted by J_{Li} and the movement of the LFP/FP interface by $M_{LFP/FP}$. The spatial Li concentration is given in grey.

The depth-averaging approximation corresponds to surface insertion of Li, shown in Figure 1.3a. In this scenario, Li traverses through the interfaces within the bulk. This has a significant impact on the model outcome, as the Li concentration within the particle quickly adjusts to the surface concentration. In contrast, the mode of bulk transport in Figure 1.3b represents a moving interface within the particle that is limited by bulk Li diffusion. Here, Li has to diffuse from the surface and inwards. The larger the particle the more limited it will be by bulk transport. In fact, experimental studies on micrometer sized LFP particles report the occurrence of both surface insertion and bulk limited transport in various directions [26]. The varying modes of Li transport can explain the large variability in reaction rate estimates and diffusivity of Li in LFP. As a consequence, depending on the particle size distribution within the electrode, different modes of Li transport can be expected.

The phase-field results of phase suppression in LFP is a good example on how computational studies can aid in understanding experiments. The model of single LFP electrode particles undergoing (dis)charge displayed the same shift in phase transition pathway found in experiments. This modelling technique has, thereafter, been applied to describe bulk mass transport limited growth in large LFP particles [27] and other phase changing materials such as $Li_4Ti_5O_{12}$ (LTO) [28]. However, these models still use simplified theories which limit the ability to quantitively compare modelling results to experiments.

For example, charge transfer is generally modelled using the classical Butler-Volmer equation for ion transfer. This formalism is known for exaggerating the rate transfer at high potentials which can lead to a faulty description of the spatial and temporal evolution of the LFP/FP interface [29]. Another important input is the free energy density that is often described by a simplified regular solution model. This model is known to inaccurately describe the energy landscape of LFP [30], most likely due to the incomplete description of short range order in the solid solution phase.

Although these phase-field models can reflect the correct trends, measuring quantitative electrochemical metrics that can be validated by experimental studies remains challenging. Bridging this gap can be achieved by incorporating more advanced theories and consistent input parameters. In phase-field modelling, this depends upon more accurate descriptions of the kinetics and thermodynamics. Quantifying the effects of these requires advanced computational studies at many scales. This is explored within this thesis.

1.2 Modelling at many scales

Depending on the time and length scales in which events take place, different types of modelling techniques can be used to better understand their underlying mechanisms. For a battery system, it could be thermal effects at the macro scale during vehicle operation, Li ion migration between electrodes, bulk and interfacial effects in single particles and ordering between atomic species on the crystal lattice. Figure 1.4 schematically presents different models of a battery system at different time and length scales.

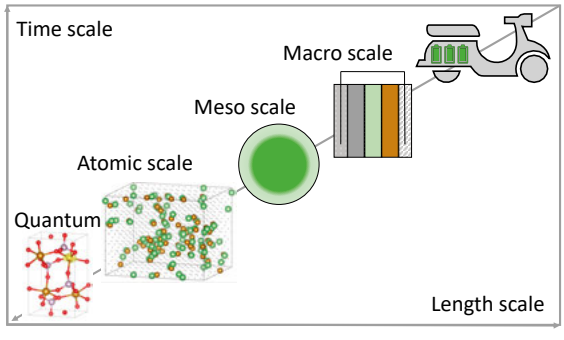

Figure 1.4. Schematics of a battery (and its context) across many scales, in length and time, starting in the north-east corner with a battery pack in an electric vehicle going down via a single battery in which Li ions move across electrodes, to single electrode particles and finally down to the atomic structure of the solid crystals that those particles consist of.

The performance of an entire battery can thus – in principle – be traced back to events occurring between atomic species. However, in practice, the situation is more complex, as a battery system is a highly intricate mix of interactions at different time and length scales. Therefore, it is advantageous to perform computational studies on model systems, where single encounters can be isolated, and their fundamental relationships and behaviours understood.

As the Li ions enter the host electrode at the Ångström scale, the crystal volume must adjust, leading to the development of mechanical strain fields

that extend over a long range. At this point, individual atoms can no longer be resolved, and the host must be viewed as a homogenized particle at the meso scale. Figure 1.5 schematically explains this concept.

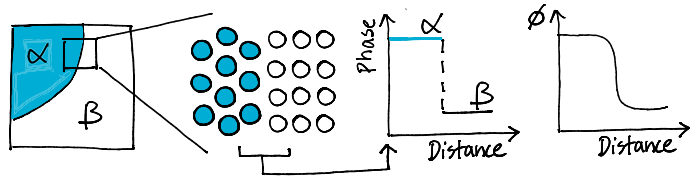

Figure 1.5. Two phases, α and β consisting of different atomic ordering and the interface between them that can be approximated as being diffuse. The atomic resolution is thus homogenized into a continuum field. By solving for the continuous variable Φ, the movement and morphology of the interface can be tracked based on gradients of concentration and chemical potential.

The concept of considering the interface as diffuse is the first ansatz in phase-field modelling [31, 32, 33]. The illustrated two phase system in Figure 1.5 has one phase-field which is described by the continuous order variable Φ. This variable takes on a constant value in the bulk α phase, 1, and another value in the bulk β phase, 0, and varies continuously at the interface. The change in the order variable describes the movement and morphology of the interface and can be determined numerically through additional partial differential equations. This avoids the computationally demanding process of tracking phase boundaries which is required in sharp-interface models.

Among the first to formulate a phase-field model to describe phase boundaries was Langer in 1986 [34]. At that time, the model could only be solved in one spatial dimension due to the lack of computational resources. This changed in 1991 with the development of both 2D and 3D models that could describe complicated dendritic patterns in solidification processes. While the methodology originates from the description of fluids and metallic systems, it has in the past 15 years also been applied to describe batteries [35, 36]. Much due to the flexibility of the model that allows coupling partial differential equations within a multi-physics framework. And so, the technique allows for simulating complex systems by solving differential equations that couple gradients of concentration and other fields, with local free energy density contributions.

A significant advantage of the formalism is that many of its input parameters can be derived from fundamental properties, creating a direct connection to the atomic scale. This in particular makes it an increasingly valuable tool for modelling the complete charge and discharge of an entire particle, enabling the evaluation of electrochemical metrics that can be meaningfully compared with experimental findings. Coupling the model to atomistic mechanisms allows for understanding the fundamental reasons behind these metrics. This can be done by first-principle models such as Density Functional Theory (DFT)

that can describe the energetics of different atomic arrangements which can be used to evaluate the free energy density.

1.3 Scope of the thesis

The nature of interactions between the species in electrode materials determines their atomic arrangements. Weak interactions create an even distribution of Li while strong interactions can result in phase separation with strain fields that, over time, lead to mechanical damage. Understanding the factors underlying Li order is, therefore, important to avoid unwanted aging effects and in the design of more efficient electrode materials.

This thesis investigates ordering effects in battery electrodes through modelling at many scales, using the LFP system as an example. The questions are: (1) what are the effects of charge transfer kinetics on the mesoscopic phase evolution? (2) how does the equilibrium thermodynamic description of the LFP/FP system affect the resulting microstructure? and (3) what insights on battery performance can we gain by investigating short range charge ordering at the atomic scale?

Different modelling techniques are used at different time and length scales. In **paper I**, I implement a meso scale phase-field model that describes long range order while comparing the effects of two charge transfer models, the classical Butler-Volmer model of ion transfer and the Marcus-Hush-Chidsey model of electron transfer. This study is performed to gain an understanding on how the rate of Li extraction can affect the phase boundary movement and morphology within an electrode particle. In **paper II**, I use the phase-field model to investigate the effect of different descriptions of the thermodynamic free energy on the evolving microstructure.

In **paper III**, first-principle models are used to quantify atomic interactions by explicit control of both ionic and electronic degrees of freedom. This is carried out to investigate the changes in the short range order between Li ions and their polarons, and to explore how these changes can influence the formation of the energy landscape. We can already at this stage see the asymmetry in the LFP system, where coordination numbers hint on the higher stability of disorder during delithiation. A higher level of disorder is present when doping the system with Mn, as is shown in **paper IV**.

In the following, I will start at the mesoscopic picture and then dive into effects arising from atomic interactions. Chapter 2 explores thermodynamic theories of solids, both bulk and interface properties. Chapter 3 presents the methods, ranging from phase-field modelling to statistical sampling using Monte-Carlo to Density Functional Theory. Chapter 4 presents the results on the LFP phase evolution. Note that the modelling techniques presented in this thesis stretch into other areas of solid state materials science beyond Li ion batteries.

2. Thermodynamics of solids

The thermodynamic free energy is an input in phase-field modelling and this chapter aims at summarizing important concepts in thermodynamics in relation to battery applications. This chapter is based on the following references [37, 38, 39], unless otherwise stated.

A solid phase of a condensed material refers to a certain arrangement of atomic species, of an internal energy characterized by the state as a function of temperature, pressure and composition. This function of state and others defined from it provide a mesoscopic average of material properties at equilibrium. In battery applications, solids are typically far from equilibrium during operation. However, the equilibrium state serves as the reference point from which the system is displaced and thermodynamics can be used to quantify the driving forces of these displacements. The Gibbs free energy, G, of a phase can be defined as such,

$$G = U + PV - TS = H - TS, \tag{2.1}$$

where U is the internal energy, H is the enthalpy, S is the entropy, P is the pressure, V is the volume and T is the temperature of the system. From a statistical point of view, the Helmholtz free energy, F, (V = 0) can be defined as the natural logarithm of the partition function Q, which is a sum of all the different arrangements i of internal energies U_i that can be found in the system,

$$F = U - TS = -RTln(Q) = -RTln\left(\sum_i e^{-U_i/k_BT}\right). \tag{2.2}$$

The states *i* can be configurational arrangements, i.e. the placement of the atoms on the crystal lattice (F_{conf}), elastic effects (F_{elast}) due to lattice distortion, vibrational effects such as displacement of atoms from their equilibrium positions, and electronic and magnetic effects where the electrons can have different spins leading to magnetic orderings of different kinds.

When there are no interactions between the species within a crystal structure, we have the case of ideal solubility. In a binary system of either Li or Va (vacancies), the Li will mix perfectly in the structure and the internal energy of mixing reduces to zero ($U_{conf}^{ideal} = 0$). The Helmholtz free energy of an ideal solution is thereby,

$$F_{conf}^{ideal} = -TS_{conf}^{ideal} = RT(cln(c) + (1-c)ln(1-c)), \tag{2.3}$$

where c is the Li composition. On the other hand, there can be interactions between the species within the solid that can lead to the growth of a new phase with a different chemical ordering. In this case, the internal energy of mixing is no longer zero and contributes with an excess term. If interactions are small, this gives the regular solution model,

$$F = RT[c\ln c + (1-c)\ln(1-c)] + \Omega c(1-c), \tag{2.4}$$

where Ω is the regular solution coefficient. This parameter accounts for the interactions between the species within the system.

During battery operation, Li ions enter the solid crystal of the electrodes, changing the arrangement of atomic species and thereby the energy landscape. And so, the free energy is a state quantity that changes during battery operation. It is connected to the operating potential of a battery cell via Nernst equation [40],

$$E_{cell} = -\frac{\Delta F}{nf}. \tag{2.5}$$

Here, f is Faraday's constant and n is the number of electrons that are involved in the process. The potential profile of a battery that undergoes phase transition is schematically illustrated in Figure 2.1a. An abrupt change in the slope of the potential profile indicates a change in the free energy as per equation (2.5). The free energy curves of each phase, α and β, are depicted in Figure 2.1b. The stability between the phases is described by the common tangent of their free energy curves F_α and F_β. This common tangent, the tie line, frames the region where both the α and β phase can coexist and defines the phase diagram in Figure 2.1c.

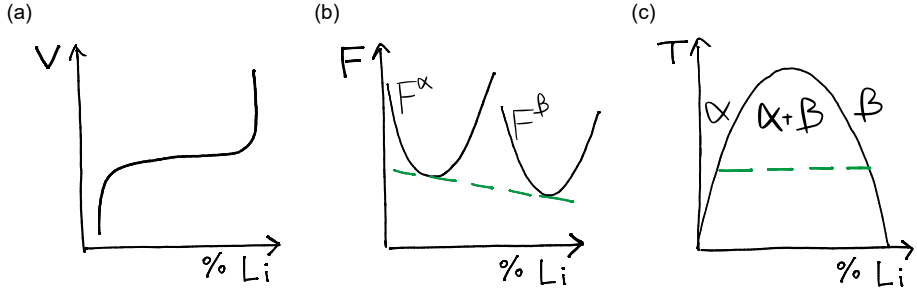

Figure 2.1. A schematic illustration of the coupling between a) a battery potential profile, b) the Helmholtz fee energy curves of phase α and β at constant temperature and c) the phase diagram. The abrupt change in slope in the potential profile during battery operation represents a change in Helmholtz free energy which happens at the onset of a phase transition. The common tangent, in green, of the free energy curves is the tie line in the phase diagram. The phases are in equilibrium within the region denoted $\alpha+\beta$.

The phase diagram is thus an important tool that can be used to better understand the phase stabilities within a system. When both phases ($\alpha + \beta$) are present in the material, they will not intermix, just like oil and water. Instead they will create regions of either the α or the β phase. This region in the phase diagram is thereby also called a miscibility gap. This region in turn can be further divided into subdomains according to the schematics in Figure 2.2.

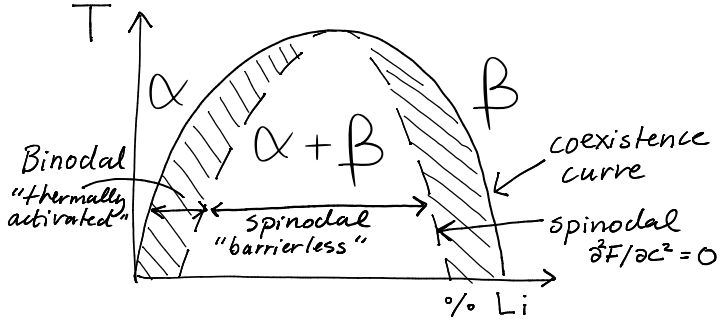

Figure 2.2. A schematic illustration of a phase diagram with a miscibility gap divided into different domains that are labelled with the appropriate terminology. Both the α and β phase are stable within the coexistence curve. The spinodal is represented by the null second derivative of the free energy and both phases can, within this region, evolve without the need for nucleation. Within the binodal, phase transition occurs when thermally activated.

The illustrative phase diagram above can be viewed as a map with coordinates of temperature and composition. At low Li composition, the α phase is most thermodynamically stable. At high Li composition, it is the β phase that is most stable. Within the coexistence curve, both the α and β phases are in equilibrium and this domain is thereby denoted with $\alpha + \beta$. This curve is defined by tie line as explained in Figure 2.1b-c. That example described the phase stability at a certain temperature. To obtain the whole miscibility gap, a free energy description as a function of temperature is necessary.

The coexistence curve also represents the concentration of Li within the α and β phase which changes over temperature. The concentration of Li is a non-conserved property during battery operation and it changes from approximately 0 % Li to 100 %. Fluctuations in the concentration field will have a certain wavelength of which their stability is defined by the second derivative of the free energy: $\delta^2 F/\delta c^2$. When this second derivative is below zero, the fluctuations become unstable and the phase transition to a two phase system occurs spontaneously. This happens within the the spinodal whose boundaries is defined by $\delta^2 F/\delta c^2 = 0$.

And so within the spinodal, phase transitions occur without the need for nucleation ("barrierless" transition). This is often called spinodal decomposition. The α and β phases are also in equilibrium between the spinodal and the

coexistence curve, in the binodal region, but phase transition can only happen here through a thermally activated process (nucleation).

The connection between the phase diagram and the electrochemical potential is therefore important. The change in potential acts as a guide when elucidating the ordering effects within the electrode materials during battery operation. An abrupt change in slope represents a new phase entering the system, of another type of chemical ordering. The (dis)charge thus proceeds with the presence of two phases within the electrode material. When two solid phases of different chemical arrangements meet, local displacement has to occur at the interface between them. Within the interface, atoms have less neighbours and thereby lower coordination. This break in periodicity thus represents an addition of energy. The system aims at lowering the total energy, and work is done to decrease the amount of interfacial area present.

The growth of the new phase depends on the free energy landscape and is governed by a chemical balance, where Li has to diffuse between phases. However, addition of Li can also lead to local displacements within the structure. In fact, insertion of Li ions into the octahedral sites of the FP structure causes volume changes and long range strain fields to emerge. The energy landscape now also changes according to the balance of forces within a mechanical equilibrium.

For an isotropic solid, the elastic free energy contribution can be defined as

$$F_{elast} = \frac{En^2}{1-\upsilon}(c-c_0)^2, \tag{2.6}$$

where E is the Young's modulus of the material and υ is Poisson's ratio [41]. To showcase the effect of this contribution in the LFP system, the free energy and corresponding phase diagram of the regular solution model with and without elasticity is presented in Figure 2.3. The energy is divided by the molar volume V_m to obtain the energy density in units J/m^3.

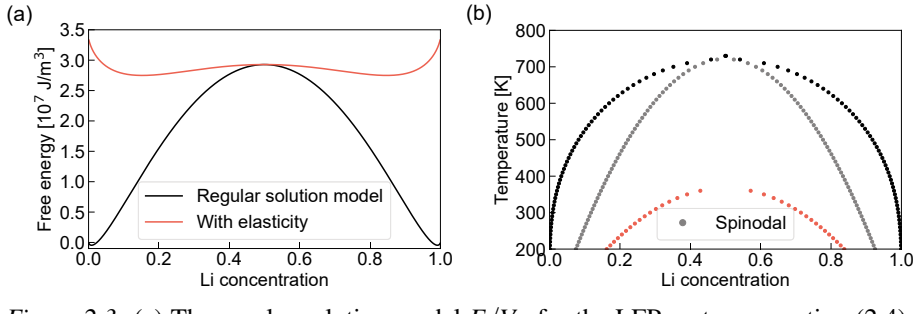

Figure 2.3. (a) The regular solution model F/V_m for the LFP system, equation (2.4), with and without isotropic elastic free energy, equation (2.6). (b) The resulting phase diagram is derived from a common tangent construction of the free energy as described in Figure 2.1b-c. Here is also the spinodal for the regular solution model defined by $\delta^2 F/\delta c^2 = 0$.

Like the illustrative phase diagram in Figure 2.2, the phase diagram for LFP depicted in Figure 2.3 contains regions in temperature and composition that describes the thermodynamic stability of different phases. At low Li content, there is the FP region and at high Li content, the LFP region. Between these is the region where both phases are in equilibrium and can coexist, FP + LFP. As can be seen in Figure 2.3, the elastic free energy contribution has a dramatic impact on the energy landscape. It decreases the energy barrier of the regular solution model as seen in Figure 2.3a and shrinks the phase boundaries of the phase diagram in Figure 2.3b.

The available experimental and theoretical descriptions of the LFP phase digram are presented in Figure 2.4. Note that the different phases are denoted by H for heterosite (FP), T for triphylite (LFP) and D/SS for disorder/solid solution.

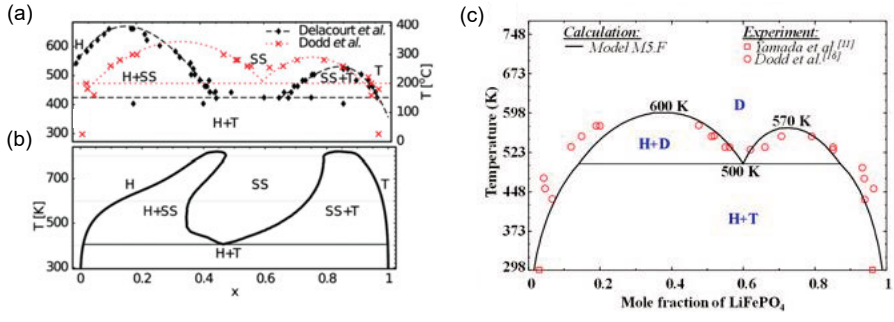

Figure 2.4. Reprints of the LFP phase diagrams existing in literature. a) Experimental phase diagrams showing the data by Delacourt et al. [16] and Dodd et al. [15] and b) the theoretically derived phase diagram by Zhou et al. [22]. Reprinted with permission from Ref. [22], copyright 2006 by The American Physical Society. (c) The CALPHAD database developed by Phan et al. [42] with data also from Yamada et al. [14]. Copyright 2019 Wiley. Used with permission from Ref. [42]. H, T, D/SS stands for heterosite (FP), triphylite (LFP) and disorder/solid solution respectively.

There are two experimental phase diagrams, one by Delacourt et al. [16] and Dodd et al. [15] presented in Figure 2.4a. Within those diagrams is the miscibility gap at low temperatures where both the LFP and FP phase coexist (H+T). There is additionally a solid solution region, SS, evolving at 423 or 473 K. The difference between these experimental phase diagrams has been attributed to the different heat treatments of the samples, where the samples by Dodd et al. were treated over longer times and can thereby be assumed to have reached equilibrium [42].

In addition, Figure 2.4b presents a theoretically derived phase diagram derived from first-principle models and Figure 2.4c presents the data from the CALPHAD database developed by Phan et al. [42]. The latter one is parametrized on both theoretical and experimental data and mimics the experimental phase diagram by Dodd et al. [15]. Overall, there are striking dif-

ferences between all these presented phase diagrams, and the one derived from the regular solution model presented in Figure 2.3b in terms of the high temperature region. The reasons for this is the description of the solid solution phase, which the regular solution model does not account for.

CALPHAD stands for CALculation of PHase Diagrams and is a methodology that relies on the thermodynamic functions of state presented in the beginning of this chapter [43]. These functions contain adjustable parameters, just like the Ω term in the regular solution model. The functions are then parameterized using experimental and theoretical data, for example heat capacities. Databases are then consecutively built on these thermodynamic descriptions for each phase within the system. For the LFP material, that is the FP, LFP and the SS (solid solution) phase.

All the presented phase diagrams in Figure 2.4 predict the stability of three phases (FP, LFP and SS) and albeit shifted in temperature and concentration, they all have the same nuances. Arguably, batteries are cycled at temperatures below 353 K (80 °C) where all these descriptions are comparable at first sight. However, differences are in fact found in the free energy curves that parameterize these phase diagrams. They are presented in Figure 2.5.

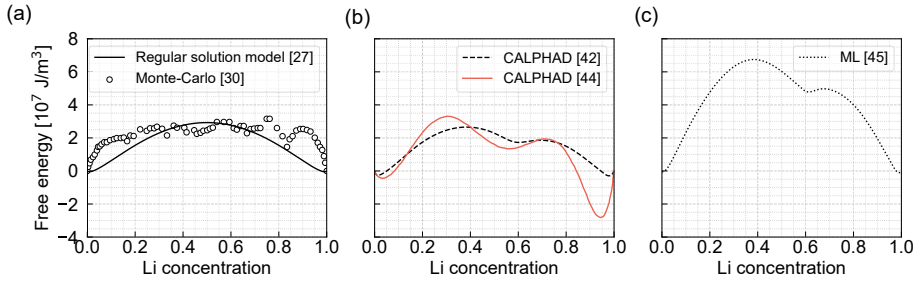

Figure 2.5. The thermodynamic free energy of LFP at room temperature from a) Monte-Carlo results utilizing a first-principle approach [30] and the regular solution model [27] parameterized on these data points, b) two CALPHAD descriptions, one by Phan et al. [42] and one by Van der Ven et al. [44] and c) ML fitting procedure from experimental phase diagrams [45].

The regular solution model, equation (2.4), is plotted in Figure 2.5a with the first-principle derived data that has been obtained through statistical sampling with Monte-Carlo simulations. The datapoints from the sampling do not directly correspond to the theoretical phase diagram in Figure 2.4b as two different Monte-Carlo algorithms were used. The regular solution coefficient Ω in equation (2.4) is derived from a numerical fit on these datapoints. While the barrier height between the energy minima is similar, the shape of the free energy is not.

Although these free energy descriptions are at room temperature, for some, traces of the high temperature solid solution phase persists, as seen by the third local minima at 50-60 % Li concentration in Figure 2.5b and c. The

CALPHAD data in Figure 2.4b gives the free energy curve in Figure 2.5b. The same figures shows another CALPHAD-like description that is less rigorous but still utilizes the Redlich-Kister polynomials common for the CALPHAD methodology [44]. Both descriptions present a third local minima at approximately 50-60 % Li that represents a metastable solid solution. Another approach presented in Figure 2.5c utilizes a minimization procedure aided by machine learning algorithms to produce free energy curves from experimental phase diagrams. This is an example of when different forms of the free energy landscapes can result in the same phase diagram.

Within the presented experimentally derived thermodynamic descriptions in Figure 2.5b-c lies a high temperature phase that is not accounted for in the simplified theory of the regular solution model. The local minima at 60 % Li and the varying height in barrier between this minima and the two global minima (at the dilute limits) hint at an asymmetry in interactions within the FP and LFP phase. It is therefore questionable if the regular solution model is enough to describe the energy landscape of the LFP system. Despite this, all phase-field models presented in the literature for the LFP system utilize this simplified model [25, 46, 27, 47, 48].

In fact, deviations from non-ideality and high interactions between chemical species are expected in battery electrodes due to the charged species involved. The positively charged Li ion and negatively charged polaron interact with long range electrostatic forces of attraction while being repelled by species of the same charge. The solid solution phase is thus also expected to have a certain degree of charge ordering. This issue has previously been reported but not thoroughly investigated [23].

At last, I'd like to touch upon the topic of kinetic effects. Many applications, such as batteries for electric vehicles, require fast charging. The rate of Li insertion will affect how the system will traverse over the energy landscape. Not only is the charge transfer rate important but also the diffusion within the solid crystal which becomes complicated in ceramic systems where multiple sublattices exists. In turn, the mobility will not only depend on the diffusion coefficient of Li but also on the energy landscape itself. This will be explained in later chapters.

3. Methodology

A phase can be defined as a chemical system with a set of atoms that have a certain crystallographic order. The atoms can be ordered in a periodic lattice or disordered. For example, atoms ordered in a face-centred cubic lattice is one phase, and a disordered liquid is another. The phases in the investigated LFP battery electrode evolve at the meso scale and are in principle characterized by interactions between Li and Fe(II) ions at the atomic scale. In this chapter, we start by looking at one particle and zoom in on these interactions. The theoretical background and computational details of the different methods used within the thesis are outlined.

3.1 Modelling the meso scale

At the meso scale, the atoms in the electrode particles are homogenized and matter is described as a continuum. The mesoscopic description in this work is based on a phase-field model developed by Tang and coworkers [49, 27].

A phase-field is a scalar field characterized by an order parameter in time and space that describes the local state by the phases present. The order parameter can be the concentration of a chemical specie, such as Li in the LFP electrode. When the Li concentration is approximately 1, we have the LFP phase, when it is 0, we have FP. The change in Li concentration over time can then describe the phase evolution within the LFP system. Assuming that J is the flux of Li atoms, the change in Li concentration c with time can be written as [39],

$$\frac{\delta c}{\delta t} = -\nabla \cdot J. \tag{3.1}$$

The flux of Li atoms is in turn defined by a mobility M and driven by the thermodynamic driving force which is the gradient in chemical potential μ,

$$J = -M\nabla\mu. \tag{3.2}$$

By replacing the flux in equation (3.1) with equation (3.2), we get the Cahn-Hilliard equation,

$$\frac{\delta c}{\delta t} = \nabla M \nabla \mu. \tag{3.3}$$

The mobility in turn can be concentration dependent and this dependency is conventionally described by considering an ideal solution. In this case, Fick's first law in the x-direction is,

$$J = -D\frac{\delta c}{\delta x}. \tag{3.4}$$

In a non-ideal solution it is defined by the chemical potential as seen earlier,

$$J = -M\frac{\delta \mu}{\delta x} = -M\frac{\delta \mu}{\delta x}\frac{\delta c}{\delta x}. \tag{3.5}$$

And so, the mobility can be defined as,

$$M = \frac{D}{\delta \mu / \delta c} = \frac{D}{\delta^2 f / \delta c^2} = \text{equation } (2.3) = \frac{D}{c(1-c)}. \tag{3.6}$$

This gives the common form of the Cahn-Hilliard equation with a concentration dependent mobility,

$$\frac{\delta c}{\delta t} = \nabla M c(1-c)\nabla \mu. \tag{3.7}$$

This version of the Cahn-Hilliard equation (eq. 3.7), is the one implemented in the phase-field model. The chemical potential in turn is the variational derivate of a free energy functional F, $\mu = \partial F / \partial c$. The free energy functional contains different energy contributions,

$$F = \int_V f_{chem} + f_{elas} + f_{grad}\, dV. \tag{3.8}$$

In this case, the functional includes the thermodynamic free energy f_{chem}, elastic energy f_{elast} and the gradient energy f_{grad} which characterizes the interface.

The thermodynamic free energy is conventionally described using the regular solution model, equation (2.4). Elastic energy is derived from the theory of linear elasticity which assumes small deformations in the material. Previously, the effect of an isotropic elastic energy was presented and discussed in relation to the phase diagram in Figure 2.3. The eigenstrains of the LFP material varies with direction and therefore contributes with an anisotropic elastic energy. This will, therefore, result in a spatially varying phase stability described by the following chemical potential,

$$\mu = \frac{\delta F}{\delta c} = \frac{\delta f_{chem}}{\delta c} - C_{ijkl}\varepsilon^0_{ij}(\varepsilon_{kl} - \varepsilon^0_{kl}c) - \kappa\nabla^2 c. \tag{3.9}$$

Here, the eigenstrains are denoted as ε and C_{ijkl} is the stiffness matrix, while κ is the gradient energy coefficient that describes the interfacial energy contribution. The mechanical equilibrium is determined by solving the strain field, σ, using equation (3.10),

$$\frac{\partial \sigma_{ij}}{\partial x_j} = \frac{\partial}{\partial x_j}[C_{ijkl}(\varepsilon_{kl} - \varepsilon^0_{kl} c)] = 0. \tag{3.10}$$

The system at hand is illustrated in Figure 3.1.

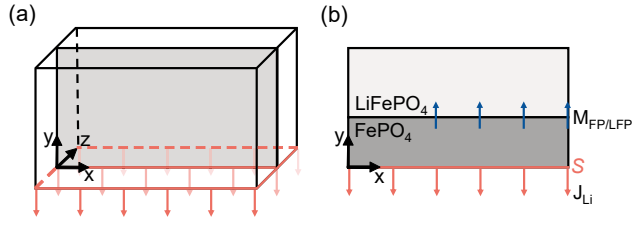

Figure 3.1. An illustration of a homogenized one particle system from which Li is extracted at the boundary S with flux J_{Li} showing a) the three dimensional system and b) a two dimensional rendering of the yx-plane. The direction of the moving FP/LFP interface is perpendicular to the surface and is denoted by $M_{FP/LFP}$.

A one particle system is considered, with an infinite Li reservoir at the particle/electrolyte interface denoted S. Charge transfer is modelled at this interface by a Neumann boundary condition. This circumvents explicit modelling of the electrolyte phase and any possible mass transport limitation that exists there. The FP phase initiates, therefore, at the electrode boundary S and moves into the bulk particle. This is the mode of bulk mass transport presented previously in Figure 1.3b.

The evolution of the Li concentration and strain field over this domain is governed by the partial differential equations, (3.7) and (3.10). However, these equations cannot be solved analytically and require numerical approaches. Among these is the Finite Element Modelling (FEM) technique that divides the system into smaller regions of finite size [50]. This constitutes the mesh which has a certain element shape and size. Each element is defined by the coordinates of its nodal points. Simple functions, so-called shape functions, are then used to approximate the unknown variables at the nodal points. These values are subsequently used to extrapolate the field over the entire mesh element and thereby the entire domain.

The FEM description requires the use of the weak form of the partial differential equations. To derive these weak formulations, the Cahn-Hilliard equation has to be further simplified. This is because it contains second- and fourth-order spatial derivatives which requires higher order shape functions in FEM. To avoid that, one can split the expression into two coupled equations to be solved separately. These two coupled equations correspond to the following:

$$\frac{\partial c}{\partial t} = \nabla M c(1-c)\nabla \mu, \tag{3.11}$$

and,

$$\mu = \frac{\partial f_{chem}}{\partial c} - C_{ijkl}\varepsilon^0_{ij}(\varepsilon_{kl} - \varepsilon^0_{kl}c) - \kappa\nabla^2 c. \tag{3.12}$$

Describing the weak form of equation (3.11) starts by first multiplying the equation with the test function w and then integrating over the domain under consideration, V [50]. Integrals containing partial derivatives can be further simplified using Green's formula (integration by parts) which reduces the order of derivatives as done in equation (3.13). The last integral term in equation (3.13) concerns the surface S while the other represents the bulk. Here, M(c) equals Mc(1-c).

$$\int_V w \cdot M(c)\nabla\cdot\nabla\mu dV = -\int_V M(c)\nabla w\cdot\nabla\mu dV + \int_{\delta V} M(c)\nabla\mu\cdot w\hat{n}\cdot dS \tag{3.13}$$

Consequently, to induce a change in concentration at the surface S, $\partial c/\partial t$, a flux on the chemical potential has to be applied. At this point, a relation between the charge transfer rate and the chemical potential is required. Fortunately, there are some electrochemical equations that handle this relation. In fact, charge transfer is conventionally modelled using the Butler-Volmer (BV) equation, defined as

$$J(\eta) = j_0\left[\exp\left(\frac{\alpha\eta}{RT/V_m}\right) - \exp\left(\frac{(1-\alpha)\eta}{RT/V_m}\right)\right], \tag{3.14}$$

where j_0 is the exchange current density, α is the transfer coefficient, and η is the overpotential at the electrode particle surface. Here, both delithiation and lithiation is conventionally assumed to be symmetric and α is defined as 0.5. The overpotential in turn is defined as the difference between the electrode potential E and the equilibrium electrode potential (E_{eq}) according to equation (3.15).

$$\eta = E_{eq} - E = \mu_{eq} - \mu - f\Delta\Phi \tag{3.15}$$

The equilibrium electrode potential is the potential when no net charge is flowing, and is defined as the equilibrium chemical potential μ_{eq}. This parameter is extracted from the common tangent of the thermodynamic free energy description, which for now remains the regular solution model. The common tangent represents the chemical potential when both the LFP and FP phases are in equilibrium. The electrode potential in turn is defined by the difference between the chemical potential μ and an externally applied potential $\Delta\Phi$.

The BV equation thus relates the electrode surface potential to ionic transfer, described by an exponentially increasing current density. This surface chemical potential is a variable that is naturally obtained from the phase-field solution. While this equation is often valid at overpotentials, it leads to a pronounced increase in current due to its exponential terms. The consequence

is, therefore, that it might strongly misrepresent the systems under study by predicting an exaggerated charge transfer rate.

In addition, the BV equation, while phenomenological, can be linked to classical transition theory of ion transfer. However, there is a coupled charge transfer of both ions and electrons during intercalation of battery compounds that is especially pronounced in the LFP system due to the localized small polarons. One can thus not assume that the electrons remain in their ground state [51]. Another relation that can be used to describe charge transfer is the Marcus-Hush-Chidsey (MHC) formulation of electron transfer [52], equation (3.16).

$$J(\eta) = \sqrt{\frac{k_B T}{4\pi\lambda}} \int_{\infty}^{-\infty} \frac{1}{1+\exp(\mathrm{x})} \exp\left(-\left[x - \frac{\lambda \pm e\eta}{k_B T} \right]^2 \left[\frac{k_B T}{4\lambda} \right] \right) dx \quad (3.16)$$

The MHC equation is parameterized with the reorganizational energy, λ, which quantifies the event when the Li ion has to reorganize its coordination shell while leaving the electrolyte to enter the electrode. This formulation showcases the curved potential plot that has been experimentally validated for the LFP electrode [29], and recently also for many other materials [53, 54, 55, 56]. Despite this, the complex integral form of the equation has limited its use. One way to circumvent the implementation of this complicated equation by employing the simplification proposed by Zeng et al. [57], presented in equation (3.17). Note that this equation is already non-dimensionalized.

$$J(\eta) \approx \tau \cdot j_0 \sqrt{\pi\lambda} \tanh\left(\frac{\eta}{2}\right) erfc\left(\frac{\lambda - \sqrt{1+\sqrt{\lambda}+\eta^2}}{2\sqrt{\eta}} \right) \quad (3.17)$$

For comparison, the current calculated using the BV and MHC equations are plotted in Figure 3.2. Note the exponential behaviour of the BV vs the plateauing of the MHC predicted currents.

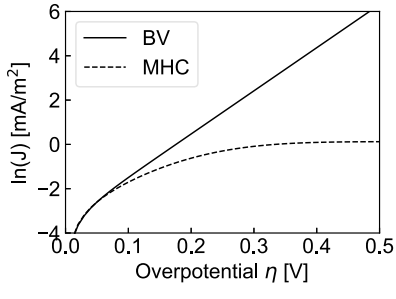

Figure 3.2. The Butler-Volmer and Marcus-Hush-Chidsey equations, with $k_0^{BV} = 2.035 \cdot 10^{-4}$, $k_0^{MHC} = 2.062 \cdot 10^{-4}$ and $\lambda = 8.3RT$ from Ref. [29].

The pre-factor of both the BV and MHC equations, the exchange current density, is related to the rate constant k according to,

$$j_0 = \frac{nf}{N_A L^2} k_0, \tag{3.18}$$

where n is the number of transferred electrons for each Li ion, N_A is Avogadro's number and L is the interface width. Here, values for k_0 and λ are taken from Ref. [29]. Furthermore, the potential in the electrochemical cell, E_{cell}, can be calculated as the difference between the LFP electrode potential and a reference electrode, which is chosen as Li metal (-3.04 V),

$$E_{cell} = E_{LFP}^{Li} - E_{Li}^{Li} = \left(\frac{\mu}{F} + \Delta\Phi\right) - E_{Li}^{Li}. \tag{3.19}$$

The current is determined by integrating the change in concentration over time.

$$I = \frac{F}{N_A L_S} \int_S \frac{\partial c}{\partial t} dS, \tag{3.20}$$

With the above presented equations, we now have a numerically consistent description of a bulk LFP electrode particle. The phase-field equations are implemented in the open-source FEM solver FEnICS [58, 59].

3.2 Modelling the atomic scale

The LFP particle has until now been considered as a continuum. Within this description lies averaged quantities of the interactions between the Li and Fe(II) species. These can be found in the free energy, the eigenstrains, the reorganizational energy and in the gradient energy term. In this chapter, we will turn to the atomistic description of LFP. As starting point, the crystal structures of FP and LFP are given in Figure 3.3.

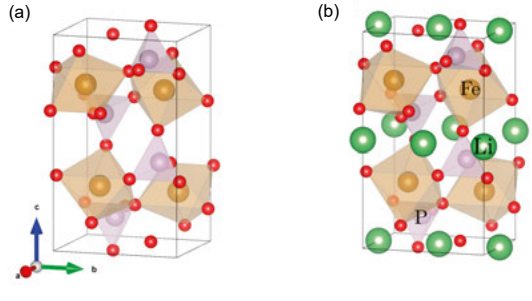

Figure 3.3. a) The FP and b) the LFP crystal structure consisting of the following species: lithium (green), iron (brown), phosphorous (purple) and oxygen (red).

3.2.1 Statistically sampling the energy landscape

The thermodynamic free energy of a system can be described by the Helmholtz free energy given in equation (2.2), which is a sum over all configurations found within the system. Imagine a lattice on which a certain amount of atoms A and B reside. The lattice is fixed expect the A and B atoms that can be interchanged, i.e. we have a [A,B]-sublattice. This is a so-called lattice gas, where movement of atoms are allowed in certain sites while the rest of the lattice remains fixed. The particles can be non-interacting for an ideal gas, or they can be interacting between nearest-neighbours or even entire subsystems. There are a manifold of different possible configurations of these atoms which depend on the size of the system, the number of lattice sites and the interactions between atom A and atom B [38].

For the LFP system, we fix the PO_4 atoms and allow for the two sublattices [Li,Va] and [Fe(II),Fe(III)]. One is between Li and Li-vacancies which we denote as Va. Another is for the two different oxidation states of Fe, +II and +III. To obtain different configurations of these species on the lattice, we can employ the Monte-Carlo technique.

Such an algorithm starts with a specified initial structure of LFP, at a certain temperature and with a certain concentration of Li- and Fe(II)-ions. A trial step is conducted, where one atom (either Li or Fe(II)) is chosen and exchanged with another atom (either Va or Fe(III)) at a new site. Both the choice of atom and the site on which it is moved are stochastically determined. The energy of the new structure, $E(2)$, is calculated and compared with the previous one, $E(1)$. The probability of accepting this state is then defined by equation (3.21).

$$\mathrm{acc}(1 \rightarrow 2) = \exp\left(\frac{E(1)}{kT}\right) - \exp\left(\frac{E(2)}{kT}\right) \tag{3.21}$$

If the probability is lower than a randomly generated value between [0,1], the state is accepted and a new trial move is attempted. Otherwise, the atom is moved back and the algorithm starts over. This ensures that the algorithm is unbiased. One trial step at a time, this algorithm will visit different states and traverse over the energy landscape. The trajectory of accepted structures reveals information about the clustering behaviour of the species in the system.

However, depending on the size of the system as well as the type and strength of the interactions between the species, capturing all configurations might require several millions of steps or even an infinite number. It is therefore impossible to reach the theoretical value of the true partition function in equation (2.2). Instead a predetermined number of steps is chosen depending on the computational efficiency of the algorithm. Two limiting factors exist, one is the efficient prediction of energy for each trial step and another is the efficient memory allocation of structural information. One way to predict energies in an efficient manner is by parametrizing an interaction model [60, 61].

In short, the interaction model predicts the energy cluster by cluster. To do so, it contains pre-determined energetic contributions of unique clusters. Therefore, for this methodology we also have to ensure that the atoms are strictly contained on a fixed lattice during the sampling procedure. This is also called lattice-based Monte-Carlo.

3.2.2 Predicting energies by clusters

The energy of a periodic arrangement of atoms can be separated into cluster contributions. Figure 3.4 presents a schematic illustration of the different clusters found within the LFP electrode material, including two-body clusters between Li-Li, Li-Fe(II) and Fe(II)-Fe(II) ions.

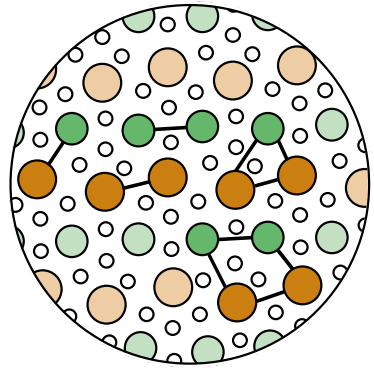

Figure 3.4. A schematic illustration of a fixed LFP framework showing a selection of pairwise clusters, triplets and quadruplets.

The whole LFP structure can be divided into pairwise clusters described with interaction parameters, $C_{a_i a_j}$, for each atomic species a_i and a_j within a cutoff radius of r_{ij}. The total energy, E, is then defined in equation (3.22), as the sum of the energetic contributions of all pairwise clusters found within the structure. The constant term depends on the composition of the configurations and is otherwise independent from the distribution of species on the lattices.

$$E = \sum_{\langle i,j \rangle} \left[C_{a_i a_j}^{r_{ij}} \right] + const. \tag{3.22}$$

Within this closest neighbour description is the assumption that the ions are perfect spheres that interact the same way regardless of direction, i.e. Li-Fe(II) interactions are identical to Fe(II)-Li interactions. However, this becomes complicated when considering larger clusters such as Fe(II)-Li-Fe(II) where the polarons do not "feel" each other if they are in the next neighbouring shell. This is a grave assumption for ionic systems that experience long range electrostatic interactions.

And so, more complicated interaction models might be necessary to accurately capture such many-body effects. For example, a three-body cluster contains a third atom and could improve the descriptions of Li-Li-Li or Li-Fe(II)-Li interactions. This can be achieved by a cluster expansion model [61, 62]. In theory, the total energies of a structure $\vec{\sigma}$ is then obtained by a sum over the energy contributions of each cluster ω [62].

$$E(\vec{\sigma}) = \sum_{\omega} J_{\omega} m_{\omega} < \Gamma_{\omega'}(\vec{\sigma}) >_{\omega} \tag{3.23}$$

The parameter J_{ω} denotes the effective cluster interaction for each cluster ω. Some clusters are equivalent by symmetry which is determined by their multiplicity, m_{ω}. The last term corresponds to the the cluster functions, $\Gamma_{\omega'}$. These functions are products of point functions of occupation variables, averaged over all clusters ω' that are equivalent to the cluster ω. Practically, the cluster expansion is truncated and it is reasonable to consider up to four-body clusters of atoms. That is generally an accurate approximation, since the interactions between atoms decreases with distance.

Usually, this holds well for metallic systems which is where the methodology also originally was developed for [63]. It does however not entirely transferable to ionic systems that experience long range electrostatic interactions. In fact, disregarding these interactions and sorely predicting energies of ionic multi-component systems based on a many-body interaction model will result in a faulty description of the clustering behaviour. Even though the prediction accuracy might be good for similarly sized systems, extrapolating to larger cells is doubtful as shown in Ref. [64]. Instead, the best interaction model was obtained when the long range interactions were captured by an electrostatic term and the short range interactions by the cluster terms. This also allowed a more sparse interaction model as lower cutoffs were needed.

The interaction model presented in equation (3.22) can therefore be improved by addition of a long range Coulomb potential determined through Ewald summation. This requires additional information on the charge q_{a_i} and q_{a_j} of atom a_i and a_j. This results in the following form of the energy,

$$E = \sum_{\langle i,j \rangle} \left[C^{r_{ij}}_{a_i a_j} + \frac{q_{a_i} q_{a_j}}{r_{ij}} \right] + const. \tag{3.24}$$

Essentially, a dataset consisting of atomic structures and their total energies can be used to fit the parameters in equation (3.24) using the CCS code [60]. All atoms within the dataset has to be mapped back to the same lattice. However, relaxation effects are still included in the energy. This model in turn is then used to predict the total energies of other structures of similar composition. So for each trial step conducted in the Monte-Carlo algorithm, equation (3.24) is called and used to predict the total energy of the resulting struc-

ture. A dataset to fit an interaction model can be prepared by conducting first-principle calculations, such as using Density Functional Theory (DFT).

3.2.3 Density Functional Theory

This section will give a summarized description of first-principle modelling and the reader is referred to Ref. [65] for a more rigorous introduction to the field. The energy of any atomic configuration can be obtained by solving the quantum mechanical wave function, the Schrödinger equation. This equation has 3N variables, where N is the total number of particles in the structure multiplied by three for each coordinate axis (x,y and z). However, an exact solution of this equation only exists for very simple systems like the hydrogen atom. To gain an understanding of the quantum properties of crystal structures, we have to further simplify the system at hand.

The first step in doing so is by considering the Born-Oppenheimer approximation, which assumes the separation of the degrees of freedom of nuclei and electrons. The reason for this is the mass of the particles, electrons are smaller and therefore move faster than the nuclei. Thus, the electronic and ionic problem can be solved separately. Despite this, the description of the electronic system remains complicated. It is now a $4N_e$-body problem, where N_e is the number of electrons and each electron can have a certain spin (up or down) and its location is still defined with three spatial coordinates. The LFP primitive cell that consists of 4 Li, 4 Fe, 4 P and 16 O has in total 304 electrons. And so, the complication still lies in the description of a many-body problem.

In 1927, Thomas and Fermi independently proposed the idea of describing the electrons as a density and in 1964, Hohenberg and Kohn laid the foundation for Density Functional Theory (DFT) [66]. In contrast to the explicit consideration of all 304 electrons in the LFP primitive cell, an inhomogeneous electron gas can be described by a certain density that is defined in space. Taking into account the electron density, therefore, simplifies the wave function to only three variables, turning it into a 3-body problem. Within the Kohn-Sham DFT description, this density $\rho(\boldsymbol{r})$ can in turn be described as the sum over orthonormal non-interacting orbitals $\Psi_i(\boldsymbol{r})$,

$$\rho(\boldsymbol{r}) = \sum_{i=1}^{N} |\Psi_i(\boldsymbol{r})|^2. \tag{3.25}$$

The orbitals are expressed as basis functions which are linear combinations of known mathematical functions. For the periodic crystal structures studied in this thesis, plane waves are chosen as they naturally satisfy periodic boundary conditions. The total energy of the electron density contains multiple contributions as seen in equation (3.26),

$$E[\rho(\boldsymbol{r})] = E^{kin}[\rho(\boldsymbol{r})] + E^{ext}[\rho(\boldsymbol{r})] + E^{H}[\rho(\boldsymbol{r})] + E^{xc}[\rho(\boldsymbol{r})] + E^{NN}, \tag{3.26}$$

where E^{kin} is the kinetic energy of non interacting electrons, E^{ext} is the interaction energy between electrons and the nuclei, E^{H} is the classical electron-electron repulsion, E^{xc} is the exchange-correlation energy depending on electron interactions and E^{NN} is the energy from the interacting nuclei. All these terms are known except the exchange-correlation energy which is approximated. The potential of this contribution will be,

$$V_{xc}(\boldsymbol{r}) = \frac{\partial E_{xc}[\rho(\boldsymbol{r})]}{\partial \rho(\boldsymbol{r})}, \tag{3.27}$$

which is used in the coupled Kohn-Sham equations below for every non-interacting orbital i,

$$\left(\frac{-\nabla^2}{2} + V_{ext} + \int \frac{\rho(\boldsymbol{r}_2)}{r_{12}} d\boldsymbol{r}_2 + V_{xc}(\boldsymbol{r}_1)\right)\psi_i(\boldsymbol{r}_1) = e_i \Psi_i(\boldsymbol{r}_1). \tag{3.28}$$

Here, V_{ext} represents the external potential from the nuclei and e_i is the electron energy for a certain electron i of the orbital $\Psi_i(\boldsymbol{r})$. This equation is iteratively solved, beginning with an initial guess for the electron density $\rho(\boldsymbol{r})$. This results in a specific set of orbitals Ψ_i, which subsequently provides a new $\rho(\boldsymbol{r})$ as described by equation (3.25). This process is repeated until the system converges within a designated error tolerance. The challenge is in defining the exchange-correlation energy and while an exact functional does not exist, there are numerous approximations for it [67].

In this thesis, I have used the Generalized Gradient Approximation (GGA) and more specifically the Perdew-Burke-Ernzerhof (PBE) functional [68]. The PBE functional describes not only the electron density, $\rho(\boldsymbol{r})$, but also its gradient, $\nabla\rho(\boldsymbol{r})$. Accounting for electron density variations is important for systems with atoms of different oxidation states, such as the Fe(II) and Fe(III) charged ions in the battery electrode material under study. The oxidation state of the ions are also determined by the valence electrons, and so the core electrons are treated through a pseudopotential. In this situation, the valence electrons are implicitly affected by this potential.

Despite this, just standard semi-local DFT with a PBE functional is still not enough to localize the electron density needed to obtain integer electron occupation. This is due to an inherent error when considering an electron density, when all electrons interact with each other they also interact with themselves which gives the so called self-interaction error. This is problematic when solving the wave function for the LFP system at intermediate Li concentrations, where the d-electrons have to be localized on certain Fe sites. The self-interaction error will instead enhance electron repulsion and promote delocalization, leading to partial occupation. This can be mitigated by treating all the d-electrons separately, which is done within the DFT+U method. Here, for each d-electron on an Fe site, a +U Hubbard correction characterizes an on-site Coulomb interaction that promotes integer occupation.

Using DFT+U, crystal structures of LFP can thus be geometry optimized by step-wise changing the atomic positions, converging the wavefunction of the electron density and calculating the total energies of the structures. The Vienna Ab initio Simulation Package (VASP) is used in all the first principle calculations presented in this thesis as it treats solid state systems using plane waves and pseudopotentials [69, 70]. However, there are still challenges when using this methodology. Even with a Hubbard +U correction, there is a risk that the electron density localizes around the points of largest structural deformations. Consequently, a system with one single Li ion will always converge to a state where the polaron is located on the closest Fe site. While this might indeed be the case at 0 K it will not allow us to capture the energetics at other charge separations that could be accessible at higher temperatures.

One way to control the localization of the charge density and thus the electronic degrees of freedom within a crystal structure, is to distort the system initially. Another is to bias the convergence of the wavefunction, using Occupation matrix control (OMC) [71]. I choose the the latter option as the OMC algorithm has been integrated within the VASP code. This allows for a standardized workflow that can easily be reproduced.

Within this workflow, atomic structures of varying sizes up to $2\times2\times2$ of the cells presented in Figure 3.3 are generated with various degrees of Li concentration. Configurations of very dilute structures, at $x_{Li} \leq 6.5$ % and $x_{Li} \geq 93.5$ % have been generated and optimized using the OMC+DFT+U methodology. These are then used to parameterize the interaction model presented in equation (3.24). All configurations are mapped to the initial unoptimized structure to ensure that all structures are fixed on the same lattice. This is schematically illustrated in Figure 3.5.

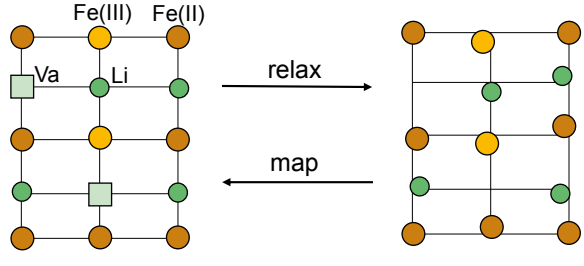

Figure 3.5. Structures of different atomic arrangements of Li, Fe(II), Va and Fe(III) are constructed and geometry relaxed using OMC+DFT+U. The resulting structure is thereafter mapped back to the same lattice which is used with the relaxed energy as part of the dataset to parameterize an interaction model. In this schematic picture, the P and O atoms are left out for visualization purposes.

The geometry optimized structures can also be used to determine the eigenstrains as input for the linear elasticity in equation (3.10). The eigenstrains are then taken as the fractional difference between the lattice parameters of the relaxed LFP and FP crystal structures [72, 27].

3.2.4 Controlling ionic and electronic degrees of freedom

Occupation matrix control (OMC) can be used to explicitly control the electron degrees of freedom by specifying the occupation matrix of the Fe ions [73, 71]. Electrons in the valence band of Fe are within the five 3d-orbitals and their occupation is represented by two 5x5-matrices, one for each electron spin. The five diagonal elements of these matrices represent the five 3d-spin density states while off-diagonal elements represent their orientation. Specifying these occupation matrices allows the control of the oxidation state and orbital occupation of each Fe site. To test this methodology, calculations were performed on the $[Fe(H_2O)_6]^{+2}$ complex in Figure 3.6.

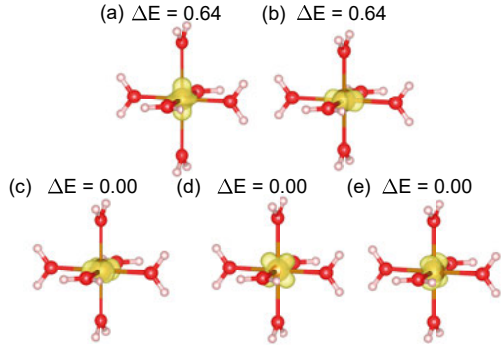

Figure 3.6. Spin densities and total energy differences, ΔE, from OMC+DFT+U calculations on $[Fe(H_2O)_6]^{+2}$ corresponding to a)-b) high energy e_g states and c)-e) low energy t_{2g} states.

The OMC approach initializes the electron occupation of the ions and resets it at each electronic relaxation step. This does not explicitly change the wavefunction or the electronic density, instead it acts as a potential which adjust the charge towards the specified occupation. A two-step procedure is utilized, the first one being a restrained relaxation with occupation control and then an unrestrained calculation without. The unrestrained calculation starts with the relaxed structure and wavefunctions from the previous step.

The magnetic moments of the Fe ions are inspected to determine if the localization is successful. Furthermore, the occupation matrix is also inspected to ensure that it does not diverge much from the original input. The eigenvalues of the occupation matrices for each atom can be used to obtain the weighted electron occupation, and thereby its oxidation state [74].

4. Phase transitions in $LiFePO_4$

Modelling techniques at many scales, ranging from Ångström to the micrometer, have been used to investigate phase transitions in the LFP battery electrode material. The spatial and temporal movement of the LFP/FP interface is modelled using the phase-field technique, where gradients of concentration and chemical potential are derived from an energy functional. Within that functional lies the thermodynamic free energy description that dictates the outcome of the intercalation process even in conditions far from equilibrium.

The first section of this chapter examines how the charge transfer rate influences the microstructural evolution (Paper I), followed by an exploration of the free energy landscape (Paper II). This landscape in turn is an effect of atomic scale interactions, and so we zoom into the short range order within the [(Li,Va), (Fe(II), Fe(III)]-sublattices (Paper III and IV).

4.1 Microstructural evolution

The battery electrode consists of porous agglomerates, of primary and secondary particles, connected by a binder and emerged in electrolyte solution. Each particle contains grains joined by grain boundaries, defects such as pores and impurities. During (dis)charge of the battery, gradients of Li concentrations will evolve, leading to different ordered and/or disordered phases within the bulk. This constitutes the microstructure.

The spatial phase evolution during (dis)charge of a battery particle is complicated to experimentally assess. Complex setups, such as in-situ Transmission Electron Microscopy (TEM), are needed to obtain imaging of particles during insertion and extraction of Li [7]. Examining partly charged particles after cell operation is dubious as those have already undergone relaxation [75]. On the other hand, electrochemical measurement of properties, such as the cell potential, gives an average that does not fully represent bulk material properties. The cell potential of the LFP battery electrode is a prime example. The onset of the phase change from LFP to FP is represented by a discontinuity in voltage, and it is then constant until the end of the delithiation process. The spatial evolution of the LFP/FP interface remains a mystery.

In this chapter, I unveil the spatial and temporal evolution of the LFP and FP phases during the delithiation process using the phase-field model outlined in section 3.1. First, I will show the effect of the charge transfer rate and then of the thermodynamic free energy description. Both the kinetics and the thermodynamics allow for spatially varying geometrical patterns that have important implications on the mechanical integrity of the battery electrode.

4.1.1 Charge transfer kinetics

To simulate the Li ions leaving the electrode during delithiation, charge transfer is modelled through a flux boundary condition. The conventional way to define this flux is through the Butler-Volmer (BV) model of charge transfer, equation (3.14), that assumes an exponentially increasing rate with respect to the electrode potential. An alternative to the BV model is to use the Marcus-Hush-Chidsey (MHC) formulation in equation (3.17) which assumes a plateauing rate. The latter one has been validated for the LFP system [29]. Therefore, simulations using the BV and MHC equations are utilized to evaluate the effect of their different current-overpotential dependence.

All the parameters used in the phase-field model are presented in paper I. The charge transfer kinetics is governed by the prefactor k_0 which is the rate constant. The MHC model additionally accounts for the reorganization energy λ. These are material specific parameters and have been obtained from Ref. [29] for the LFP system. For the BV model, $k = 2.035 \cdot 10^{-4}$ and for the MHC model $k = 2.062 \cdot 10^{-4}$ and $\lambda = 8.3$RT. Simulations have been conducted at different applied potentials $\Delta\Phi$ and rate constant magnitudes $k = k_0 \cdot (1 - 10^5)$. The size of the system is 128x64 nm if not otherwise stated.

The impact of coherency strain between the LFP and FP phase is evaluated by conducting simulations with and without accounting for the strain in the free energy functional. In the case of no strain effects the interface remains planar as seen in Figure 4.1.

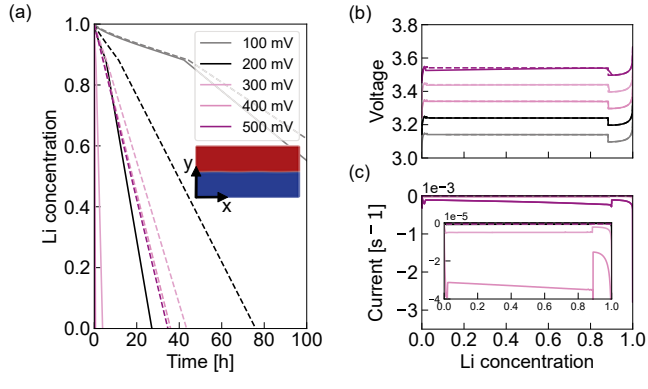

Figure 4.1. Phase-field simulations at $k/k_0 = 1$ and with different applied potentials, $\Delta\Phi$, without coherency strain showing a) the change in Li concentration with time, b) the voltage profile and c) the current I/FN_A. The dashed lines represent the MHC model while solid lines correspond to BV. Snapshot of the microstructure shows the LFP phase in red and FP in blue.

There are many interesting aspects of these simulation results that are important to point out. First, as seen in Figure 4.1a, the delithiation process is faster with higher applied potentials and more so when using the BV formulation. This is expected as the BV formulation has an exponentially increasing

charge transfer rate. The simulations using the MHC equation reach a limit at 400 mV which represents the plateau in Figure 3.2.

Second, the voltage profile in Figure 4.1b abruptly changes as the FP phase is introduced. The cell potential is calculated according to equation (3.19) and is connected to the variable chemical potential that changes as a function of the thermodynamic free energy and the gradient energy term. The discontinuity in cell potential seen in Figure 4.1b at around 90 % Li is attributed to the energy needed to introduce a new interface to the system. In fact, while not shown here, simulations conducted for larger system sizes give a smaller discontinuity in voltage, as the ratio of the interfacial contribution to the total energy decreases.

Third, the snapshot of the microstructure shows the LFP phase in red and the FP phase in blue coexisting with a planar interface that is perpendicular to the flux direction. In reality, it is the x-direction that experiences the most coherency strain and such a planar interface is therefore not expected. The results from the conducted simulations with coherency strain at different charge transfer rates are presented in Figure 4.2. Snapshots of the phase distribution from the simulations are given in Figure 4.3.

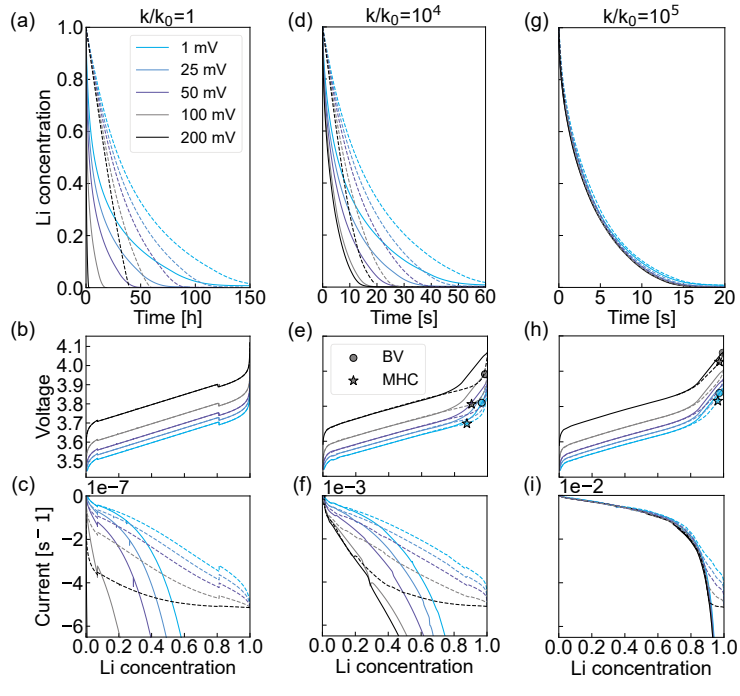

Figure 4.2. Simulations at different charge transfer rates and applied potentials showing a,d,g) the change in Li concentration over time, b,e,h) the voltage profile and c,f,i) the current I/FN_A. The dashed lines represent the MHC model while solid lines correspond to BV. When no discontinuity is present at the onset of phase transition, scatter points are included instead.

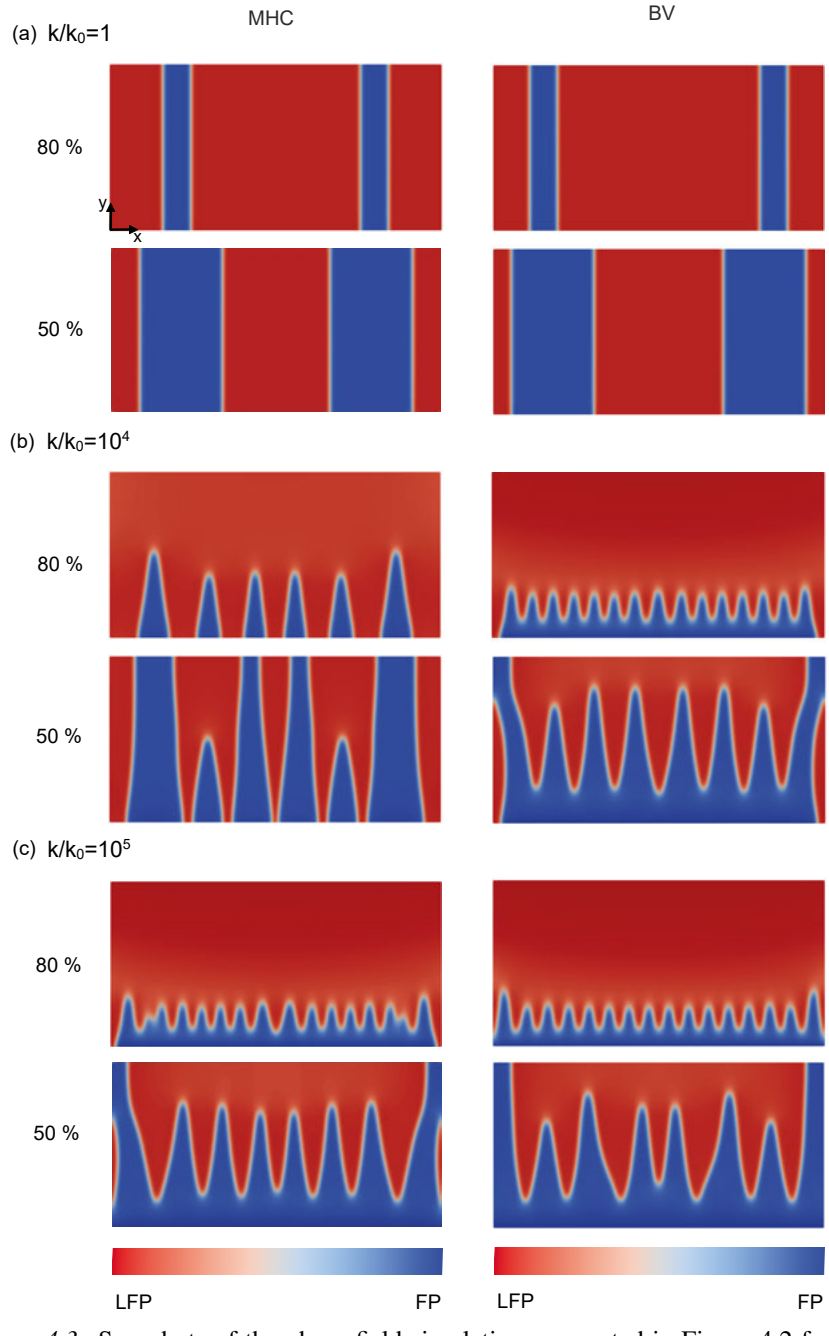

Figure 4.3. Snapshots of the phase-field simulations presented in Figure 4.2 for the applied potential $\Delta\Phi = 100$ mV at 80 and 50 % Li content for the three different charge transfer rate magnitudes a) $k/k_0 = 1$, b) $k/k_0 = 10^4$ and c) $k/k_0 = 10^5$.

The effect of the coherency strain in the phase-field simulation is striking. This could already be seen in the phase diagram of the regular solution

model, Figure 2.3, where the Li solubility increased for both the LFP and FP phase and the energy barrier decreased. Furthermore, the coherency strain contributes with an additional term to the chemical potential as seen in equation (3.9), and so, lower applied potentials are necessary to reach similar overpotentials as in the case without strain.

The change in Li concentration with time as shown in Figure 4.2a,d,g is more pronounced and the system delithiates faster. Mass transport limitation is reached at charge transfer rate $k/k_0 = 10^5$. At this stage, further increasing the Li flux at the boundary has no effect and both the BV and MHC simulations converge to the same result. The voltage profiles in Figure 4.2b,e and h are also different as compared to the system with no coherency strain. The cell potential varies with concentration instead of being constant as previously seen in Figure 4.1b. This is also observed in other studies and has been linked to the effects of the elastic free energy [44, 46].

Interestingly, this discontinuity is not present at charge transfer rate of $k/k_0 = 10^4$ and $k/k_0 = 10^5$, Figure 4.1e and Figure 4.1h, respectively. Instead scatter points have been included at the point of phase transition. To understand the reason for this, one has to go back to the origin of the cell potential defined by equation (3.19). The voltage of the LFP electrode is defined by the chemical potential that varies with Li concentration. The energy landscape is described by the equilibrium phase diagram, that is characterized by the solubility lines and the spinodal as illustrated in Figure 2.2. Two types of phase transitions are possible here, a first order and a second order phase transition. Between the coexistence curve and the spinodal, phase transitions occur by overcoming an activation barrier (first-order) and are characterized by nucleation and subsequent growth. Within the spinodal this barrier ceases to exist (second-order).

These two types of transitions can also be examined by considering the discontinuities in the derivatives of free energy. At the phase transition point, a discontinuous first derivative indicates a first-order transition, while a continuous first derivative but a discontinuous second derivative indicates a second-order transition. This definition can be used to directly distinguish between different types of transitions through the simulated voltage profile, revealing which parts of the energy landscape are being accessed.

To summarize, coherency strain modifies the energy landscape and directly affects the temporal and spatial phase evolution. Higher rate of Li removal induces a shift from a first order to a second order phase transition where there is no need for nucleation. Depending on the choice of flux boundary equation, different microstructural outcomes are expected. The BV formulation predicts the phase transition point to happen earlier in concentration but converges to the MHC results at the point of mass transport limitation. It is noteworthy however that the BV model reaches this point already at a rate constant that is one order of magnitude lower as compared to the MHC model. From this point one, the MHC formulation will be the model of choice when describing charge transfer in the phase-field simulations.

4.1.2 Impact of the free energy landscape

There are a variety of different thermodynamic free energy descriptions of the LFP system in literature and they have been previously presented in Figure 2.5. First principles studies have produced a broader form of the chemical free energy as compared to the regular solution model [22]. Other studies suggest that the thermodynamic description, fitted to experimental data, exhibits an asymmetrical free energy form with a third local minimum at 60 % Li [42, 44]. This third local minimum corresponds to the solid solution phase that is present at around 420-470 K in the equilibrium phase diagram in Figure 2.4. Despite the varying thermodynamic descriptions, all published phase-field models utilize the regular solution model [25, 46, 27, 47, 48].

There are three design requirements to the implementation of an energy description in the developed phase-field model. (1) The energy has to be differentiable and thereby continuous, (2) it has to be limited at the boundaries and (3) it has to have continuous derivatives. One of the reasons for the widespread use of the regular solution model is that it is easy to implement and fits all three requirements. The Li fraction is naturally limited between [0,1] due to the natural logarithms. These terms also also ensures a mathematical smoothness and its first and second order derivatives are both continuous.

Another reason for its widespread use is the lack of open source data in the literature. While there are indeed multiple studies presenting varying forms of the free energy, the data are not easily accessible. Either the parameters are lacking [44], or a minimization procedure has to be conducted [45], or a database implemented [42].

To circumvent these challenges, datapoints are directly extracted from the published studies and spline interpolations are utilized to obtain continuous piecewise functional forms of each free energy description. These functions are then directly implemented in the phase-field model described in section 3.1, to test their effect on the phase evolution in LFP. The three free energy descriptions that are implemented are presented in Figure 4.4 with their corresponding datapoints and spline functions.

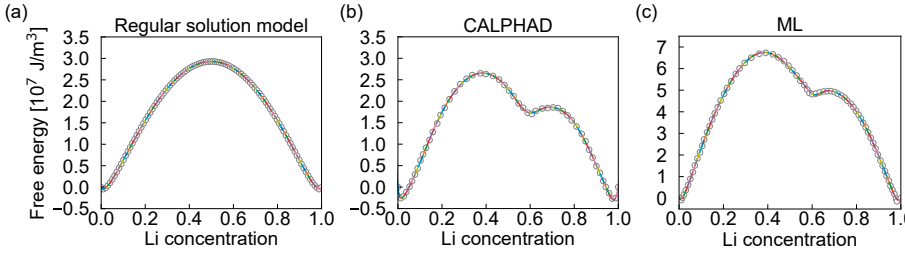

Figure 4.4. Scatter points and spline functions of three free energy descriptions, a) the regular solution model, b) the CALPHAD description by Phan et al. [42] and c) the ML description by Lund et al. [45]. Note the different scaling on the y-axis.

The spline functions are presented together in Figure 4.5 with their respective derivative, with and without the effect of isotropic elastic energy (equation (2.6)).

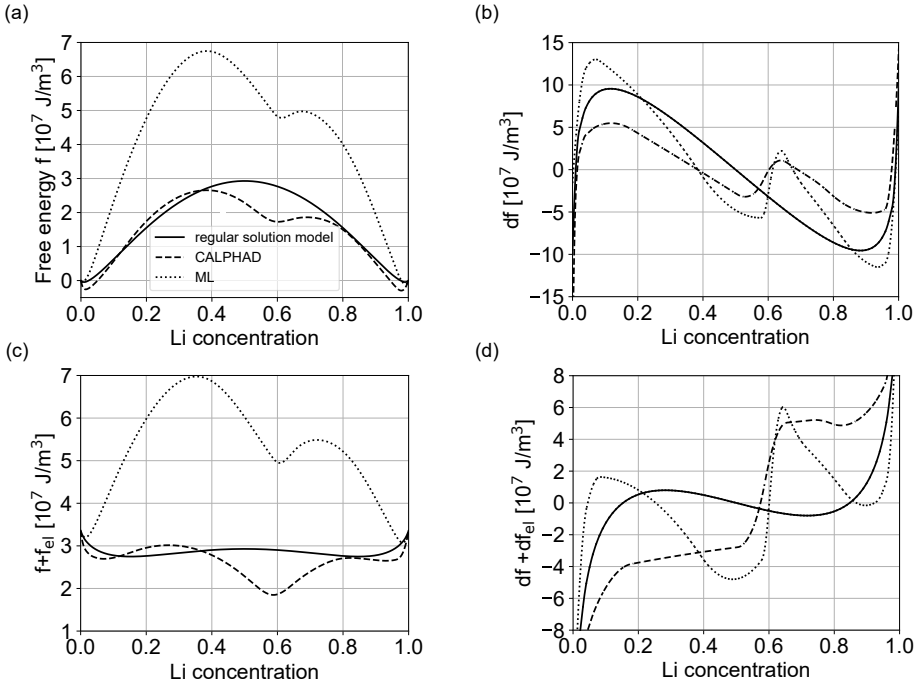

Figure 4.5. All spline functions presented in Figure 4.4 with their respective derivative, with and without isotropic elastic energy at room temperature. a) The free energy of the regular solution model [27], the CALPHAD description [42] and the ML model [45]. b) The first derivative df, c) the free energy with the elastic energy contribution $f + f_{el}$ and d) the derivative of both contributions $df + df_{el}$.

The CALPHAD free energy and the regular solution, Figure 4.5a, have approximately the same barrier height. However, the CALPHAD description has additionally a third local minimum at 60 % Li concentration that corresponds to the metastable solid solution phase. This minimum is also present in the ML derived free energy, that also has more than double the barrier height between the FP and LFP phase as compared to the other models.

One can already at this point start hypothesizing the possible outcomes in the phase-field model. Lets start without considering coherency strain by looking at Figure 4.5a and 4.5b. The first derivative of the free energy shows two energy barriers, one between the LFP-SS and one between SS-FP. For the CALPHAD model, the minima between the LFP and SS phase are particularly close in energy.

Lets consider the case when coherency strain is included through isotropic elastic energy, in Figure 4.5c and 4.5d. This has a considerable impact on the

energy landscape. The local minima at 60 % in the CALPHAD description now becomes a global minima, and one should therefore expect this phase to evolve. The first derivative of the CALPHAD free energy with elastic energy showcases a stepwise function, and one can thus expect a consecutive transition i.e. LFP to SS, and SS to FP.

Results from the phase-field simulation without coherency strain using the regular solution model and the CALPHAD description is presented in Figure 4.6. The ML description gets stuck at 97 % Li and does not evolve further than that, likely due to the high energy barrier.

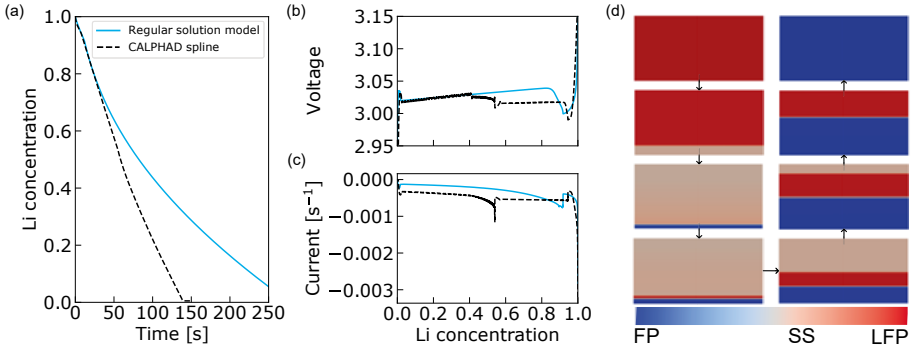

Figure 4.6. Phase-field simulations without coherency strain utilizing the regular solution model and the CALPHAD free energy description. Charge transfer is modelled using the MHC equation with rate constant $k/k_0 = 10^4$ and applied potential $\Delta\Phi = 100$ mV. The results show a) the change in Li concentration over time, b) the voltage profile, c) the current I/FN_A and d) snapshots from the simulation using the CALPHAD free energy showing the evolution of three phases, LFP, FP and SS (solid solution).

Despite using the same flux condition, the change in Li concentration in the system (Figure 4.6a) decreases faster in the simulation utilizing the CALPHAD free energy. Both the voltage profile and the current (Figure 4.6a and 4.6b) show a discontinuity at the onset of a phase transition, which happens twice for the simulation utilizing the CALPHAD description. Snapshots of the microstructure shows the initiation and evolution of a phase with approximately 60 % Li content. This is the third local minima in the free energy, presented in Figure 4.5.

This minimum represents the solid solution phase in the phase diagram in Figure 2.4 and is denoted here with SS for solid solution. It is only when the SS phase has filled the system that the FP phase is initiated. At the SS/FP interface, the LFP phase is formed and the delithitation proceeds through the movement of these three phases in a layered manner.

Simulations with coherency strain are also conducted at higher charge transfer rates and presented in Figure 4.7. When coherency strain is assumed between the phases, both the temporal and spatial evolution of the phases is different. Previously, the simulation using the CALPHAD resulted in signif-

icantly faster delithiation at $k/k_0 = 10^4$ as compared to the regular solution model. This is not as pronounced when coherency strain is considered in the phase-field model.

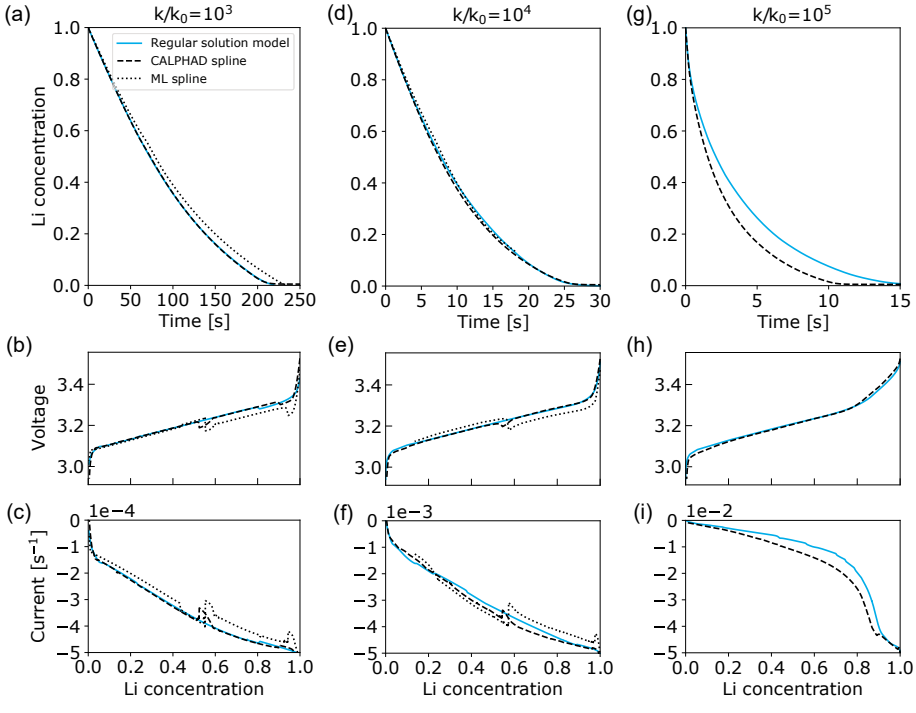

Figure 4.7. Phase-field simulations with coherency strain using different free energy descriptions; the regular solution model, the CALPHAD description and the ML description. Charge transfer is modelled using the MHC equation at applied potential $\Delta\Phi = 100$ mV. The plots show the a,d,g) change in Li concentration, b,e,h) voltage and c,f,i) current I/FN_A at three different charge transfer rate magnitudes. The simulations using the ML description do not fully converge at $k/k_0 = 10^4$ and $k/k_0 = 10^5$.

Similarly to the simulations without coherency strain, a discontinuity is associated to the phase change from SS to FP. While the temporal evolution is the same at $k/k_0 = 10^5$ in Figure 4.7d, the spatial phase evolution is not. The snapshots of the microstructures presented in Figure 4.8 shows the delithiation proceeding consecutively, first from the LFP to SS phase and then from SS to FP. At even higher rates, $k/k_0 = 10^5$, all three phases coexist (see Figure 4.9) and the delithitation process proceeds faster than in the regular solution model (Figure 4.7g) bypassing its limit of mass transport.

Snapshots of the phase evolution at charge transfer rate $k/k_0 = 10^5$ are presented in Figure 4.9, with the Li concentration field and corresponding strain field. The strain magnitudes are higher for the simulation using the regular solution model as compared to the CALPHAD free energy description. The

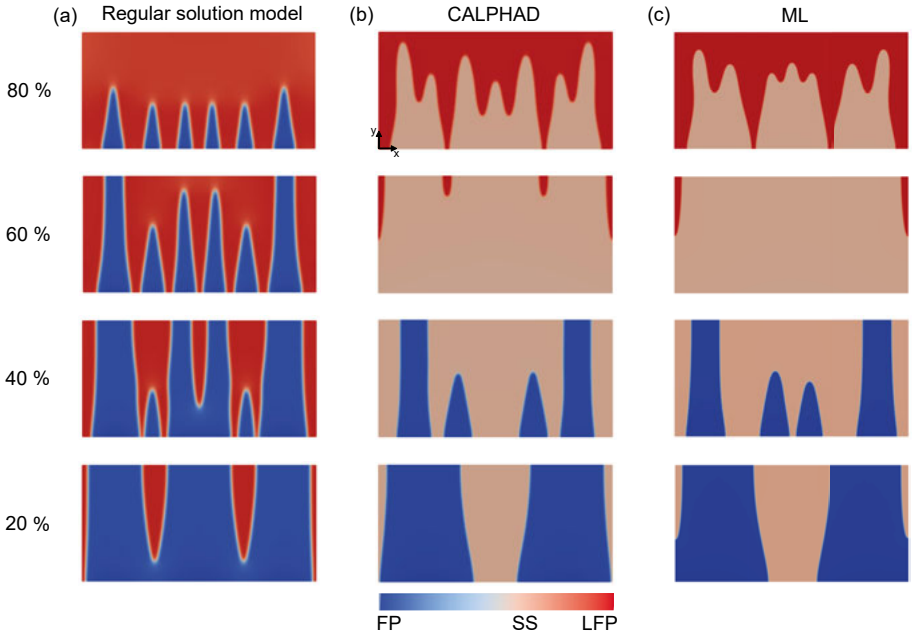

Figure 4.8. Snapshots from the phase-field simulations with coherency strain presented in Figure 4.7 at $k/k_0 = 10^4$ charge transfer rate. a) Regular solution model, b) CALPHAD and c) ML at 80, 60, 40 and 20 % Li concentration.

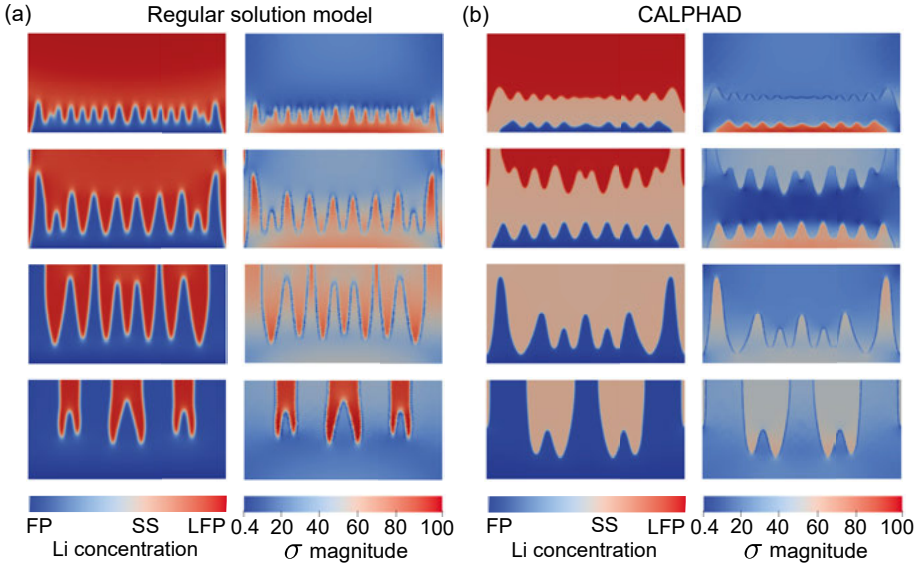

Figure 4.9. The phase evolution using the a) regular solution model and b) the CALPHAD free energy description at $k/k_0 = 10^5$ charge transfer rate, presented in Figure 4.7. At 80, 60, 40, and 20 % Li concentration with snapshots of the Li concentration field and the corresponding strain field σ.

solid solution mitigates the high strain that exists between the LFP and FP phase that would otherwise have grave implications on the mechanical stability of the electrode over time.

The existence of a solid solution phase in the LFP material has long been attributed to a size effect, where the surface to volume ratio decreases the path of Li diffusion. From a modelling perspective, the assumption of a depth-averaging approximation where Li is inserted though the phase boundary, as schematically illustrated in Figure 1.3a, has thereby become the standard approach to simulate the evolution of this solid solution phase. However, the situation is more complicated.

Numerous experiments have yielded conflicting results about the development of a metastable solid solution phase in LFP. Electron microscopy has revealed narrow disordered interfaces, measuring 4 nm wide, in micronsized particles [5]. In contrast, high resolution in situ TEM has shown an atomistically sharp FP/LFP interface in similarly sized particles [76]. Conversely, real-time in situ neutron powder diffraction on a commercial LFP electrode, also with large particles, has demonstrated the simultaneous presence of all three phases [77]. However, in relation to this study, it is challenging to ascertain whether all three phases are present within the bulk particles, or if they are distributed among different particles. For instance, some particles might solely exhibit the solid solution phase, while others display the LFP or FP phase.

The coexistence of all thee phases within the bulk particles has however been shown in other studies. In situ TEM studies on LFP nanowires with a diameter of 200-400 nm show the spatial evolution of the solid solution phase from the electrode surface, measuring 20-25x20-40 nm in size, and the existence of all three phases within the bulk material [7]. A more recent study using soft X-ray tomography present three phases in particles 300 nm wide, where a mixed phase at 30-70 % Li concentration lies in between regions with either FP or LFP [78]. The latter study shows striking similarities to the modelled microstructures presented in Figure 4.9.

The solid solution phase in the phase-field model evolves purely as a thermodynamic effect and should thereby even be present in larger particles. It is important to point out that the diffusion coefficient and mobility is the same in all the simulations and this is purely an effect of the change in thermodynamic driving forces. When more complex free energy descriptions are used, that are based on experimental findings, we see the consecutive evolution of phases, LFP to SS to FP. At mass transport limitation, all three phases are present. The energy landscape thus affects the delithiation process even at kinetic conditions that pushes the system far from equilibrium.

This study shows a simple way of implementing thermodynamic data within phase-field models by spline interpolations. However, smaller mesh size and timesteps are needed to converge the solution when using the spline functions as compared to the regular solution model. Running the simulations required

more computational resources, which might become problematic if larger system sizes are needed or when conducting 3D simulations.

To summarize, I have looked at the effect of kinetics and thermodynamics on the phase evolution in the LFP electrode material. Long range ordering of Li gives rise to geometrical patterns over the mesoscale. The evolving microstructure is an effect of the driving forces of the free energy landscape that is being traversed at different rates. For battery electrode materials, this property becomes even more important due to the complex interaction between charged species which eradicates the use of simple theories like the regular solution model.

4.2 Ordering at the atomic scale

A variety of free energies for the LFP electrode have been evaluated within a mesoscopic description and shown to strongly affect the microstructural evolution. The free energy descriptions parameterized on experimental data (Figure 4.5) show a highly asymmetric from with a third local minima. The barrier is higher from 0 to 60 % Li compared to 60 to 100 % Li. This implies that the SS phase is more accessible during the delithiation process. The stability of these phases can be evaluated by analysing the short range order between the species at the atomic scale. This is based on the hypothesis that lower short range order between Li-Li and Li-Fe(II) ions indicates higher levels of disorder.

In this section, I investigate the dilute limits of the phase diagram to evaluate whether there is more or less short range order in the LFP or the FP phase. For the LFP phase, this is done by introducing 6.25 % Li-Fe(II) pairs in an otherwise empty FP crystal ($Li_{0.0625}FePO_4$) and evaluating their clustering behaviour. At the other end of the phase diagram, I introduce the same amount of Va-Fe(III) pairs in an otherwise full LFP crystal ($Li_{0.9375}FePO_4$).

Statistically sampling these systems requires an efficient way of calculating energies of various configurations within these crystal structures. This has been achieved by generating first-principle energy-structure data of different Li-Fe(II) and Va-Fe(III) configurations. The data is used to fit two interaction models, one for $Li_{0.0625}FePO_4$ and the other for $Li_{0.9375}FePO_4$, to account for any potential interaction differences within these systems. These are used in conjunction with the Monte-Carlo method to perform simulations at constant temperature within the range of 200-1000 K.

4.2.1 Fitting an interaction model

During the statistical sampling procedure, atoms will be swapped and energies need to be calculated in an efficient manner. To fit the parameters of the interaction model presented in equation (3.24), structure-energy data is required

where the Li-Fe(II)/Va-Fe(III) are separated at various distances. Figure 4.10 shows the LFP crystal structure and the relevant distances between the atoms within the closest neighbouring shell.

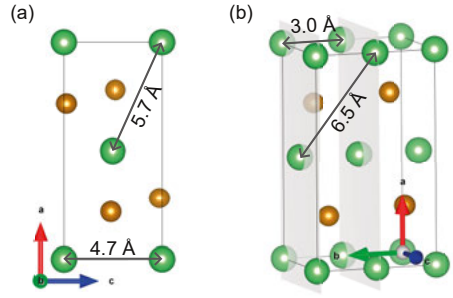

Figure 4.10. The crystal structure of $LiFePO_4$ with (a) the ac plane and (b) a three-dimensional rendering of multiple such ac planes. Lithium is shown in green, iron in brown while oxygen and phosphorus have been excluded for visualization purposes.

The procedure for the Li-Fe(II) system is identical to that of the Va-Fe(III) system. Therefore, to maintain clarity, only the former will be described in detail. A $2\times2\times2$ supercell of the structure shown in Figure 4.10 has 32 Li sites. Emptying the cell with Li and only allowing one Li-Fe(II) pair corresponds to a Li concentration of 3.125 %. Within that system are 16 symmetry non-equivalent configurations of different Li-Fe(II) pair separations. The energy of these configurations have been obtained using first-principle calculations as outlined in sections 3.2.3 and 3.2.4, by first localizing the polarons using OMC and then relaxing the structure with DFT+U.

In addition, to account for Fe(II)-Fe(II) and Li-Li interactions, configurations with two Li-Fe(II) pairs are generated. One example of such a configuration is presented in Figure 4.11. Here, the energy from the DFT+U optimization is the lowest due to the electron smearing, leading to non-integer occupation of two Fe sites. In contrast, the OMC procedure localized the electron on the chosen Fe sites.

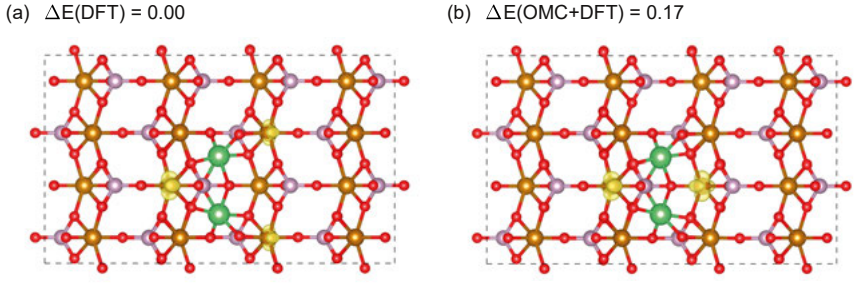

Figure 4.11. A $2\times2\times2$ LFP supercell with the d-electron density shown in yellow with energy in eV obtained using a) DFT+U where one of the electrons is smeared over two sites and b) OMC+DFT+U where the electrons are localized on two different sites.

The energies of the aforementioned 16 configurations with one Li-Fe(II) pair are presented in Figure 4.12a. The positivity charged Li and negativity charged Fe(II) interact electrostatically, and the further they are from each other the higher the energy. Separating Va-Fe(III) requires higher energies than when separating Li-Fe(II), as seen in Figure 4.12b. This already alludes to more cluster formation between the Va-Fe(III) species.

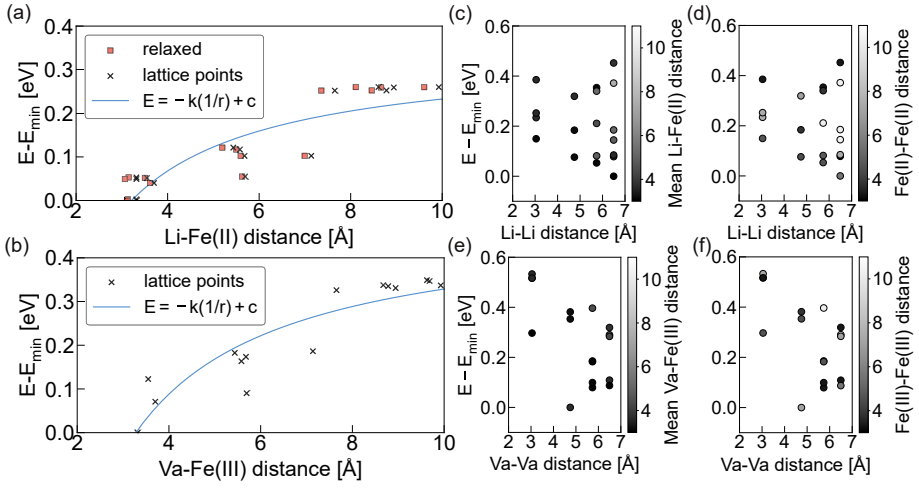

Figure 4.12. The change in energy with Li-Fe(II)/Va-Fe(III) separation in a 2×2×2 supercell with a-b) one Li/Va and one Fe(II)/Fe(III). A Coulomb relation, E=-(k/r)+c, where r is the distance between Li/Va and the Fe(II)/Fe(III), is applied to the lattice points to guide the eye. Note that fitting this curve does not account for the periodicity of the supercell. c-f) The relative energy when another Li-Fe(II)/Va-Fe(III) pair is added.

To guide the eye, a curve with the parameters E=-(k/r)+c is successfully parameterized on the energy and distance data in Figure 4.12a-b. This confirms that there is, indeed, strong long range electrostatic interactions within this system, and accounting for a Colomub potential is therefore necessary in the interaction model. By adding another Li-Fe(II)/Va-Fe(III) pair, the number of possible configurations increases, leading to a significant variation in energy, as shown in Figure 4.12c-f. Two interaction models are generated, one for the Li-Fe(II) data and the other for the Va-Fe(III) data and the parameters are presented in Table 4.1.

The electrostatic interaction parameter Q is higher in the Va-Fe(III) interaction model than in the Li-Fe(II) case. This indicates that there is an increased level of electrostatic interaction within this system. The Q parameter is also connected to the dielectric constant through $\varepsilon = 1/Q^2$, giving a value of 6 for Va-Fe(III) and 15 for Li-Fe(II). The lower the dielectric constant the higher the response is to an external electric field, and so one can expect there to be varied short range order within these systems.

Table 4.1. *Fitted parameters in the interaction model described in equation (3.24) in Section 3.2.2 for the Li-Fe(II) and Va-Fe(III) systems.*

r_{cut} [Å]	a_i	a_j	C [ev]	a_i	a_j	C [ev]
3.5	Li	Li	0.01	Va	Va	0.13
4.2	Fe(II)	Fe(II)	0.19	Fe(III)	Fe(III)	-0.05
4.0	Li	Fe(II)	-0.01	Va	Fe(III)	-0.02
4.0	Li	Fe(II)	0.04	Va	Fe(III)	0.07
4.0	Li	Fe(II)	0.10	Va	Fe(III)	0.03
$Q = q_{Li} = -q_{Fe(II)} = 0.26e$				$Q = -q_{Va} = q_{Fe(III)} = 0.33e$		

In short, the DFT+U results already allude to a difference in the short range order between Li-Fe(II) and Va-Fe(III). It is, however, not clear how this will affect the clustering behaviour as temperature changes. Neither is it apparent if there is indeed a significant difference between these two systems. Among the questions that remain unanswered in literature (see Paper III) is if the electrostatic interaction is so strong that Li-Fe(II) and Va-Fe(III) always remain closest neighbours. This is something that can be evaluated by statistical sampling. Here, atoms will be swapped leading to a trajectory of different atomic arrangements. The coordination sphere of the different species within these arrangements will inform us on the short range order.

4.2.2 Coordination between Li-Li and Li-Fe(II)

The parameterized interaction models can now be used during the Monte-Carlo simulations to sample different arrangements of the Li/Va and Fe(II)/Fe(III) species. A 4x4x8 supercell consisting of 1984 Li sites is used in the sampling procedure. Two systems are built, one with 6.25 % Li-Fe(II) pairs and the other with 6.25 % Va-Fe(III) pairs (93.75 % Li). Initially, the cells undergo 2 million trial steps for equilibration, followed by data generation in the subsequent 200 000 steps. One accepted configuration is given in Figure 4.13 from which one representative cluster is extracted.

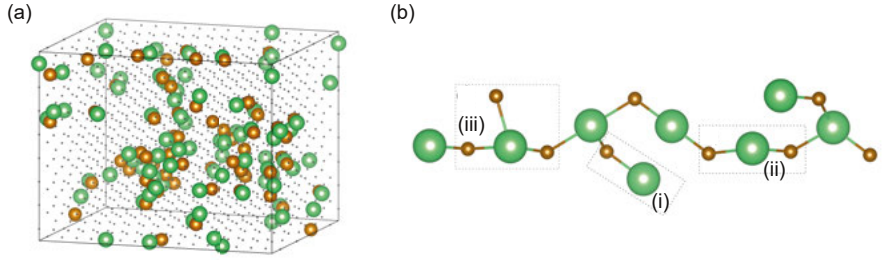

Figure 4.13. a) An accepted configuration of the sampled 4×8×8 supercell and b) a representative cluster within the configuration showing i) 1 Fe(II)/Li, ii) 2 Fe(II)/Li and iii) 3 Fe(II)/Li coordinated atoms within 4 Å.

The cluster in Figure 4.13b showcases three different coordination types that can be found in the supercell, 1 Fe(II)/Li, 2 Fe(II)/Li and 3 Fe(II)/Li. The accepted configurations in the trajectory are analysed by counting how many of each specie A is within a certain cutoff distance to specie B. This has been done for all the simulations conducted at constant temperature within the range of 200-1000 K. This gives the coordination plots in Figure 4.14.

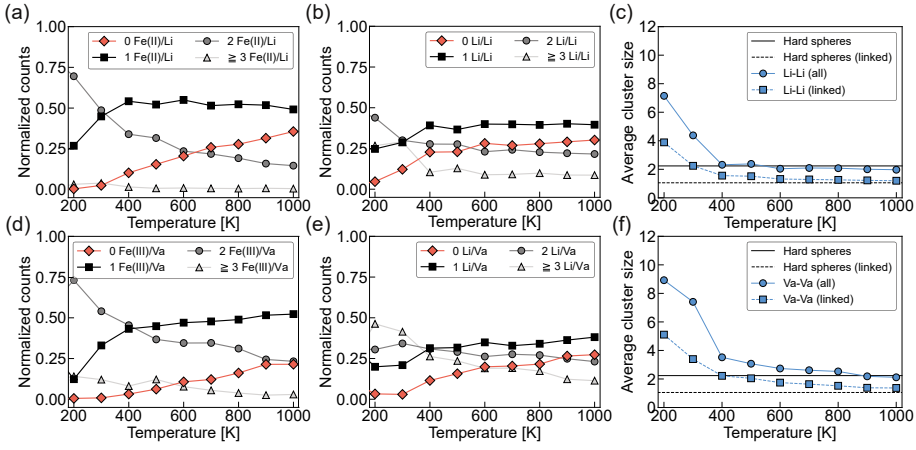

Figure 4.14. Coordination between a) Fe(II)/Li at cutoff distance 4 Å, b) Li/Li at cutoff distance 7 Å, d) Fe(III)/Va at cutoff distance 4 Å and e) Va/Va at cutoff distance 7 Å. The average cluster sizes for both systems are presented in c) for linked Li-Fe(II)-Li clusters and unlinked Li-Li clusters and f) for linked Va-Fe(III)-Va clusters and unlinked Va-Va clusters.

The content presented in Figure 4.14 is quite extensive and requires careful examination. Let us have a look at the Li-Fe(II) and Va-Fe(III) coordination in Figure 4.14a and Figure 4.14d respectively. There are a significant number of isolated Fe(II) within the cutoff distance of 4 Å. This proves that not all Li are paired with a polaron. The amount of isolated Fe(III) in the opposite case is approximately half of that. There is also a larger amount of 2 and 3 coordinated Fe(III)/Va clusters. As temperature increases, the number of smaller coordinated clusters increase at the expense of the larger ones.

Let us examine the Li-Li and Va-Va coordination in Figure 4.14b and Figure 4.14e. In these figures, a significantly higher number of 3 Va/Va clusters compared to 3 Li/Li can be observed. One such representative cluster has previously been presented in Figure 4.13. The Li/Va are linked with Fe(II)/Fe(III) creating long linear chains. The average size of these clusters are presented in Figure 4.14c and 4.14f. Both quantified with and without consideration of the linking Fe(II)/Fe(III) ions. As a reference, a simulation is conducted within the same supercell but with so-called hard spheres i.e. a non-interaction lattice gas. As temperature increases the Li-Li and Va-Va clusters converge to the

size of the ones found in this reference, approaching disorder. The average size of the Li-Fe(II) clusters are smaller than the Va-Fe(III) clusters.

The first-principle data confirmed that the interactions between Li-Fe(II) and Va-Fe(III) were different. In this section I asked the question whether these differences would lead to any significant variation in short range order with temperature. The coordination plots between the species in the different systems establish that this is indeed the case. And so, one should expect an asymmetric energy landscape as suggested in the free energy descriptions from the CALPHAD and ML models presented previously [42, 44, 45].

There are two important takeaways from this study: (1) there is high order within the solid solution phase which might explain the local energy minima associated to it and (2) the Li-Fe(II) has lower short range order than Va-Fe(III). This implies that accessing the solid solution phase is easier during delithiation.

4.2.3 The effect of doping

The clusters found in the LFP system consisted of alternating Fe(II)-Li-Fe(II) pairs. The Fe(II) acts like glue that holds the Li together. Weakening this glue would decrease the amount and size of clusters. However, the strength of the interaction between Fe(II) and Li is an intrinsic property that cannot be changed. One way to affect the orderings is to introduce another glue that attracts Li. This is done by doping the system.

A vast number of studies have explored various dopants within the LFP system. One such dopant is manganese (Mn) and an addition of small amounts have been shown to enhance both the mechanical [79] and kinetic properties [80, 81, 82]. Moreover, Mn doping has shown to induce more solid solution and the theoretical phase diagram of 10 % Mn content shows all three phases (FP, LFP and SS) at room temperature [83]. The amount of Mn content varies, and around 5 and 3 % has shown to give optimum rate performance [84, 85]. While high Mn concentrations, even up to 80 %, are currently the subject of extensive research, they have not been included in this study [86].

Similar to the undoped LFP study presented in section 4.2.1, DFT+U with OMC has been utilized to obtain structures of different atomic configurations of Mn doped LFP. One of the Fe ions within the $2\times2\times2$ LFP supercell is exchanged with an Mn ion, giving an additional sublattice of (Mn,Fe). The Mn ion can, in this environment, have two possible electronic configurations with oxidation states +II and +III. Mn(II) has an electronic configuration of $3d^5$, similar to Fe(III). In turn, Mn(III) is $3d^4$ with two unpaired electrons, leading to atomic structures exhibiting strong Jahn-Teller distortion [87]. The strong distortions the structure experiences is also the reason why the electrode material $LiMnPO_4$ is still unattainable as a battery electrode.

Four datasets are generated, containing either one or two Li-polaron pairs which corresponds to a content of 3.125 and 6.25 % Li. One Fe ion is exchanged with an Mn ion which corresponds to 3.125 % doping, and it has either the oxidation number of +II or +III. The energy of the structures in the dataset is presented in Figure 4.15a. The scattering in energies within each dataset shows the variation in configuration, where larger distances between the Li-polaron pairs induce higher energies.

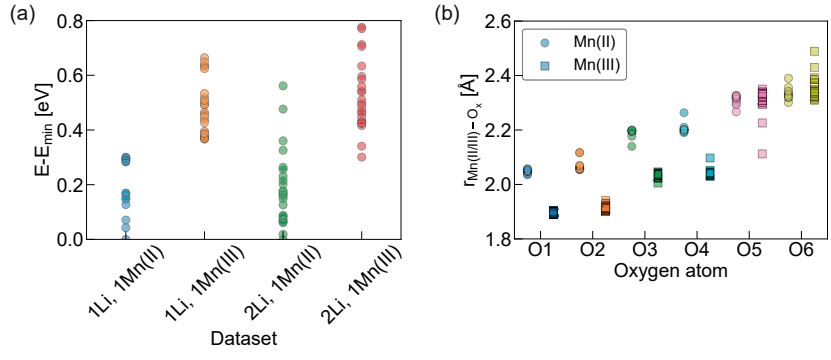

Figure 4.15. a) Scatter plot comparing the DFT+U energies of systems with one Li and one Mn(II), one Li and one Mn(III), two Li and one Mn(II) and two Li and one Mn(III). Lowest energies are obtained for Mn(II). The one and two Li datasets are normalized separately. b) Mn(II)-O and Mn(III)-O bond lengths between the six closest neighbouring oxygen atoms for the different datasets presented in a.

It clear from these results that the Mn ion prefers the +II oxidation state as those structures are overall lower in energy. One of the reasons for this can be explained by Figure 4.15b that shows the distances between the Mn ion in all structures to its six closest oxygen atoms. Longer distance between the closest oxygen atom (O1) and the farthest oxygen atom (O6) indicates a higher distortion in the crystal structure which correlates with the reported Jahn-Teller activity of the Mn(III) ions [87]. This implies that this system might experience higher strain if completely delithiated and puts a limit on the capacity of the battery electrode.

From this point on, the Mn ion remains in its +II oxidation state in the subsequent modelling approaches. Similarly to the undoped $2\times2\times2$ LFP data in Figure 4.12a, the dataset containing one Li-Mn(II) pair has 16 symmetry non-equivalent configurations of varying pair separations. The computed interaction energies for these configurations are presented in Figure 4.16 together with the results from the corresponding undoped LFP system.

The interaction is found to be enhanced in the case of Li-Mn(II) as compared to Li-Fe(II). As discussed earlier, this was also the case for the Va-Fe(III) separation which ended up inducing more Va-Va and Va-Fe(II) clustering. We can thus already hypothesize that the Li-Mn(II) might interact more favourably than Li-Fe(II). To understand how this will be accommodated in a bigger su-

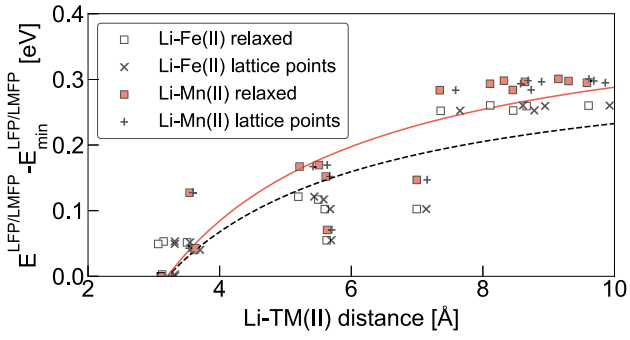

Figure 4.16. The change in energy with Li-polaron separation in which the polaron is either located on an Mn site (k = 1.36, c = 0.42) or on an Fe site (k = 1.1,c = 0.34). Coulomb potentials parametrized by E=-(k/r)+c, where r is the distance between Li and the TM(II), are applied to the lattice points to guide the eye. Note that this fitting does not account for the periodicity of the supercell.

percell with more Li-polaron pairs and varying temperatures, statistical sampling is once again employed. A new interaction model, equation (3.24), is generated for this system with sublattices [(Li,Va), (Fe(II),Fe(III),Mn(II)].

Using the CCS code to fit these parameters, the effective electrostatic interactions are described by a single effective charge factor Q. Consequently, the electrostatic interactions for Li-Li repulsion, Li-Fe(II)/Li-Mn(II) attraction, and Fe(II)-Fe(II)/Mn(II)-Mn(II) repulsion are identical. It obtains a higher value of 0.31e as compared to the undoped system with 0.26e. This correlates well with the higher energies with separation seen in Figure 4.16.

That the electrostatic interaction is the same for the Li-Fe(II)/Li-Mn(II) is clearly not represented by DFT+U data in Figure 4.16. This will not be problematic for the short range clusters as the energies are also calculated by consideration of the short range two-body corrections $C_{a_i a_j}$. However, configurations where an Fe(II) and an Mn(II) are at intermediate distances from a Li ion will be considered equal even though the energy is higher for the Mn(II) case.

The LMFP system with 6.25 % Li, 3.125 % Mn(II) and Fe(II) is statistically sampled using the same conditions as in the previous study of undoped LFP presented in section 4.2.2. Previously, the polaron was allowed to change position with the sublattice (Fe(II),Fe(III)) which is logical as the electron can hop between iron sites. However, the Mn(II) is an ion in a fixed framework and a choice has to be made on its degrees of freedom. Should the Mn(II) ion be allowed to freely be exchanged with Fe(II) and Fe(III)? or should it remain fixed?

The assumption that Mn remains fixed in its lattice position can be debated. At low temperatures, in which the batteries are cycled, one can indeed assume that the probability of Mn diffusing into another site is low. However, the process of Li insertion and extraction has been theoretically hypothesized

to majorly affect the microstructure of bulk electrode particles through grain boundary migration [88]. If entire grains shift, then so can dopants. Indeed, cation migration and mixing is a challenge in many electrode materials [89]. The distribution of dopant elements might then be entirely different in an aged battery electrode.

Both these possibilities are therefore tested in this study. One set of Monte-Carlo simulations are conducted where the Mn ions remain fixed in a disorderd manner and the sampled sublattices are [(Li,Va), (Fe(II),Fe(III))]. Another set of simulations are conducted where the position of Mn ions is freely sampled within the [(Li,Va),(Fe(II), Fe(III), Mn(II))] sublattices.

The average size of linked Li-TM(II) clusters found within the Monte-Carlo trajectories are presented in Figure 4.17. Results from the scenario where Mn remains fixed in a disordered state is shown in Figure 4.17a and when they are allowed to exchange site in Figure 4.17b. Here is also the results from the undoped LFP system and a reference state with linked hard spheres. This reference describes the same system but where the species do not interact, a so called lattice gas.

Overall, the clusters are smaller in the Mn doped system and converges to

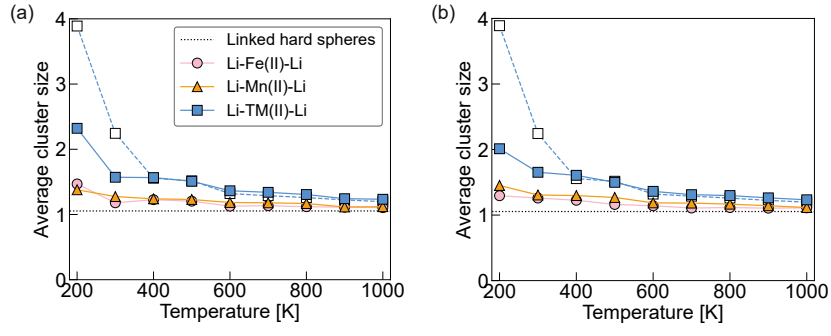

Figure 4.17. The average size of linked Li-TM(II)-Li clusters with temperature in LMFP and LFP where a) the Mn are fixed in a disordered manner and b) the Mn position is sampled. The uncoloured markers and dashed line represents the LFP system. The dotted reference line represents a hard sphere model where there are no interaction between the species.

approximately the same size at 400 K. In short, Mn doping of LFP induces less clustering at low temperatures and thus more disorder within the system. This corresponds well with the experimental studies that show more solid solution [81] in Mn doped LFP and the theoretically derived phase diagram at 10 % that predicts both the FP, LFP and SS phases at room temperature [83].

This effect can be attributed to two factors. (1) The increased electrostatic repulsion between the negatively charged Mn(II) and Fe(II), thereby inducing a disordered Mn(II) arrangement. (2) The preference for Li-Mn(II) interactions instead of Li-Fe(II). This results in a higher spread of Li within the system and thereby overall more disorder.

5. Conclusions and future work

This doctoral dissertation explores ordering effects and their impact on the microstructure evolution of energy storage materials. The material under study is the LFP electrode that undergoes phase separation during Li insertion and extraction. The thesis begins with the description of an electrode particle as a homogenized continuum and dives into the atomic arrangements of the crystal structure that it consists of.

Several computational techniques at many scales have been used to better understand the system at hand. One important objective has been to reach commercially related scales where different physical theories can be coupled to describe phase boundary movement within the mesoscale. This has been done by developing a phase-field model that describes the spatial and temporal evolution of phase boundaries during Li extraction. The following questions were stated at the beginning of this thesis: (1) what are the effects of charge transfer kinetics on the mesoscopic phase evolution? (2) how does the equilibrium thermodynamic description of the LFP/FP system affect the resulting microstructure?
The following conclusions answer these questions.

- The MHC model of charge transfer gives slower delithiation rates but ultimately converges to the same results as the BV model when reaching mass transport limitation. This point is reached by the BV model at a rate constant that is one order of magnitude lower.
- High rates result in more and sharper phase boundaries and thereby more coherency strain. This can ultimately affect the mechanical integrity of the particle.
- The description of the energy landscape has a paramount effect on the microstructure and the delithiation rates. Accelerated rates are entirely attributed to an increased thermodynamic driving force.
- An intermediate solid solution phase described by a third local minima evolves and mitigates the coherency strain within the system.

The first research findings outlined within this thesis confronts the use of different models of charge transfer. The MHC model predicts a lower charge transfer rate as compared to the BV model, which results in overall a slower delithiation process. And so, the microstructural phase evolution will be different depending on the choice of the model and the rate constant. These are

two extreme cases, the BV model of ion transfer and the MHC model of electron transfer. However, the true rate of charge transfer might lie in between when considering coupled ion-electron transport. Future work should thereby consider implementing the coupled ion-electron theory outlined in Ref. [51].

I then go on to confront the use of the regular solution model, a simple theory of weak interactions in a binary system. It is widely used despite the many other free energy descriptions for the LFP system presented in literature, each with its distinct characteristics. One step towards understanding the importance of these characteristics is to evaluate their effect within the mesoscopic description. To tackle this, I developed a framework that extracts and fits datapoints with spline interpolations that subsequently are used in the energy functional of the phase-field model. All the free energy descriptions that are based on experimental data showcases a third local minima in the free energy landscape. This minima describes the highly metastable solid solution phase and has a profound effect on the outcome of the simulations. For the first time, I could show the spatial evolution of the solid solution phase without considering enhanced Li transportation as a size effect.

Now, at this point in my research journey I wondered about the reason behind the form of the energy landscape and whether it is reasonable. In contrast to the experimentally derived thermodynamic descriptions, the only available theoretical free energy in literature did not showcase this third local minima. I thereby wanted to also investigate the atomic scale interactions, to evaluate the degree of order within the system. I asked the question, (3) what insights on battery performance can we gain by investigating short range charge ordering at the atomic scale? My research have condensed into the following answers.

- The interaction between the Li and its localized charge compensating electron (the small polaron) interact electrostatically.
- There are significant numbers of isolated polarons in the system despite the aforementioned electrostatic interactions.
- The difference between the Li-Fe(II) and Va-Fe(III) interactions and clustering degree hint at an asymmetry in the LFP energy landscape.
- There is a higher degree of charge ordering and cluster formation between Va-Fe(III) as compared to Li-Fe(II). This indicates that accessing the solid solution phase is easier during delithiation.
- Adding a low amount of Mn dopants within the structure gives a higher spread of Li and thereby a higher degree of disorder.

The first principle calculations conducted on the LFP system were challenging. Despite the use of a +U Hubbard correction in the DFT approach, it proved difficult to localize electrons on specific Fe sites, and more so when they were far away from Li. The reason for this is the strong electrostatic in-

teractions between them. Utilizing the OMC methodology was a major leap in this direction as it allowed for electron localization without the use of more complicated DFT functionals that require more computational resources. With this methodology, the energetics of different configurations of Li-Fe(II) and Va-Fe(III) could now be quantified. Statistically sampling this system showed substantial short range order and so called linked clusters were found consisting of ordered Li-Fe(II)-Li chains. These interactions were weaker as compared to the Va-Fe(II) case and so smaller Va-Fe(III)-Va chains existed.

And so, there is an asymmetry in interactions at the dilute limits of the phase diagram. The ease at which the Li-Fe(II) and Va-Fe(III) chains can be unlinked can explain the ease of obtaining disorder within the system. In this case, the Li-Fe(II) interactions are weaker which implies the possibility of accessing more disorder at high Li concentration and thereby during Li extraction. The easier it is to break up these clusters, the easier it is to obtain the solid solution phase. This will ultimately enhance the battery cycling rate and mechanical stability as seen in the phase-field model, where higher rates and lower strains are now possible.

To further advance this methodology, a more complex interaction model can be developed for example by using the cluster expansion method outlined in section 3.2.2. Especially for evaluating different dopants, such as in the case for Mn, including three body interactions might become even more necessary at higher concentrations. This would allow the description of short range order across the whole composition range. Ultimately, obtaining reliable statistical data over different configurations over the entire composition and temperature range of interest could allow the theoretical evaluation of the free energy landscape. This would circumvent the use of extensive experimental data generation and thereby an accelerated materials discovery.

To summarize, this work has advanced the knowledge of battery electrode materials but also on materials modelling overall. It confronts the use of simplified theories that once established, tend to persist simply because they are familiar and have been repeated over time. The LFP battery electrode material showcases many complex phenomena, making it an excellent material to benchmark against. Plenty of exciting work remains to explain all of its marvellous characteristics.

6. Acknowledgement

I would like to thank my supervisors, Peter Broqvist and Daniel Brandell, who trusted me in my endeavours. To Peter for cultivating the space for scientific debates and who taught me valuable skills in computational chemistry. To Daniel for believing in our ambitions, even through they might not always have made sense. Thanks also to Jolla Kullgren for his expertise in and enjoyment of atomic scale modelling. Part of this work would not have been possible if not for Nana Ofori-Opoku who taught me the phase-field technique and always had time to engage in fun scientific discussions. A big thank you to Carelyn Campbell for organizing our meeting, and all the amazing people at NIST.

My years at the Ångström laboratory have been marked by many people that I have enjoyed the company of. I would like to thank Kersti Hermansson for valuable conversations and feedback. Anders Eriksson, Jolla Kullgren, Melania Kozdra, Fabian Schwarz and Amber Mace for proof reading parts of this thesis. Many thanks to all the past and present PhD students and postdocs for the good atmosphere around the fika table. Among them being Jorge, Ageo, Neeha, Heyin, Fabian, Casimir, Babsi and many many more. I will greatly miss the Friday lunches with Klara and the fun discussions with my office mate Tove.

I also felt great support outside academia from friends and family that lent me an ear whenever I was having a hard time. Special thanks to Amanda Wood for relentlessly cheering me on and giving me great advice. I am also lucky to have met a great friend in Frederike Monsees, which whom I can share my struggles with regarding academia and life outside of it. The formatting of most my figures have been quality assessed by Jonathan and Eric, with whom I have had some great dinners with.

Life outside of academia has been filled with fun activities, I especially enjoyed the trips with Annie, Josefin, Line, Amanda and Leo as well as the gettogethers with Doris and Frida. I will look back to all the fun visits to Taps with Melania, Thijs and Daniel A. as well as the fish wine with Kinge and Le Anh. A special thanks goes to Ash, and who helped me prioritize towards the end. To all the friends that I met during my travels and who have stuck with me, among them Nynke, Lea, Anna and Flore. Thank you for all the fun times, for cheering me on and coming to Uppsala for my dissertation.

I feel ready for my dissertation much thanks to Sebastian, for providing me with food so that I could dedicate my days writing this thesis. For making life more fun and keeping my spirits up and fighting. Thanks also to Yvonne and Bengt for all the encouragement and to Fredrika for helping me plan the dissertation party.

Lastly, I would like to thank my parents, Montaha and Muwaffak, that this thesis is dedicated to. For their encouragement, love and support. For all their hard work and effort whilst coming to Sweden and their relentless drive to see my siblings and I succeed in life. Thanks to my siblings, Domiyan, Ghazwan, Riman and Rami, whom I look up to and admire.

Uppsala 23 February, 2025

7. Populärvetenskaplig sammanfattning

I takt med rådande klimatförändringar blir effektiv lagring av energi från förnybara energikällor alltmer kritisk. I det här sammanhanget har laddningsbara batterier visat en god energilagringsförmåga och har därmed viktig plats i dagens energisystem. Ett laddningsbart batteri är genialt i sin enkelhet: positivt laddade joner rör sig mellan två elektroder, vilket genererar en elektrisk ström. De laddade jonerna kan dock stöta på olika problem under sin resa, och materialen de passerar kan själva genomgå både kemisk och mekanisk skada. Syftet med detta projekt är att undersöka sådana fenomen med hjälp av beräkningskemi.

I ett modernt laddningsbart batteri lagras energi genom inkorporering av positivt laddade joner i fasta kristaller. Joner är positivt eller negativt laddade atomer och en kristall består av atomer som är ordnade på olika sätt, på ett så kallat gitter. Hur ordningen ser ut på gittret beror på vilka typer av atomer det är, hur stora de är och hur de interagerar med varandra. När joner träder in i kristallen på Ångström-skalan (10^{-10} m) måste kristallvolymen justeras, vilket leder till töjning som sträcker sig på långt avstånd. Vid denna punkt kan enskilda atomer inte längre upplösas, och kristallen betraktas som en partikel på mikrometerskalan (10^{-6} m).

En elektrod i ett toppmodernt batteri består av en mängd sådana partiklar. Prestandan för hela batteripaketet kan - i princip - spåras tillbaka till händelser som sker mellan atomer. I praktiken är situationen mer komplex, då ett batterisystem är en mycket avancerad blandning av olika material med interaktioner och händelser som sker på olika tids- och längdskalor. Till exempel så leds värme över långa avstånd, som värmen jag känner från datorn precis nu när jag skriver denna text på tangentbordet. Däremot så går det betydligt snabbare för en Li jon att röra sig från en plats till en annan i ett kristallgitter. Därför är det fördelaktigt att utföra beräkningsstudier på modellsystem, där enskilda möten kan isoleras, och deras fundamentala relationer och beteenden förstås.

Beräkningsstudier har utförts på elektrodmaterialet $LiFePO_4$ (LFP). Under urladdning av ett sådant batteri rör sig Li joner in i elektroden, och materialet omvandlas till en Li-rik LFP fas och en Li-fattig FP fas. Mellan dessa faser finns nu en fasgräns. Detta kan liknas vid en blandning av olja och vatten. Både oljan och vattnet är i vätskeform men de kan inte beblandas. Istället bildar de öar med antingen olja eller vatten. Elektrodmaterialet LFP är ingen vätska utan är i fast form, och även fast materia kan uppvisa olika typer av faser. Kortfattat representerar en fas en typ av ordning på atomär nivå. När Li sen ska förflytta sig i materialet, måste det ske genom att fasgränsen förflyttar

sig. Detta är ett långsamt förlopp i jämförelse med ett material där Li kan flytta sig dit den vill, utan att någon särskild ordning måste ställa in sig.

Elektrodmaterial som genomgår en fasförändring leder alltså till öar av den ena eller den andra fasen, vilket i sin tur gör att det går relativt långsamt att ladda ett batteri. Trots detta så är det här materialet väldigt intressant. Förutom Li så består materialet också av järn och fosfater som finns tillgängliga i riklig mängd i jordskorpan. Det gör LFP till ett ypperligt bra batterimaterial i jämförelse med många andra kommersiella batterier som innehåller höga halter av koboltkobolt. Kobolt är ett ämne som behöver fasas ut då det ofta bryts på oetiska grunder och skapar oro utifrån socioekonomiska och geopolitiska grunder.

Men hur kan man göra för att få LFP elektroden att ladda snabbare? Faktum är att den fasförändring som tidigare beskrivits, inte sker vid höga temperaturer. Vid ungefär 200 °C dyker det upp en ny fas, en löslighetsfas. Tänk nu att Li jonerna nu istället blir som karamellfärg som späds ut i vatten. Då behöver inte atomerna ställa in sig i en ordning, och inga fasgränser behöver upprätthållas. Men att använda ett batteri under så höga temperaturer är inte aktuellt då de flesta batterier används vid rumstemperatur.

Däremot så har man listat ut att om man gör partiklarna tillräckligt små, ända ner till nanostorlek (10^{-9} m) så går det att erhålla denna löslighetsfas vid höga laddningshastigheter. Det har man kunnat förklara genom att bygga en matematisk fasfältsmodell som beskriver hur fasgränser förflyttar sig i material. När Li joner kan fylla partikeln genom att transporteras via fasgränserna så kan mängden Li i materialet snabbt jämna ut sig (precis som karamellfärg i vatten!). Om det går långsamt så ordnar sig istället Li i öar av LFP fasen (såsom olja i vatten).

Att det däremot bara är storleken och sättet som Li transporten sker på som gör att man kan få en löslighetsfas, det stämmer inte. Fasfältsmodellen som har använts för att beskriva hur Li lägger sig i öar av LFP baseras på ett energilandskap. Det här landskapet kan liknas vid de svenska fjällen, med dalar och berg. Den vanligast modellen som kan beskriva det här landskapet är den så kallade reguljära lösningsmodellen som antar att bergskedjan endast består av en topp omgiven av två dalar. När Li kommer in i partikeln, så rör vi oss från den ena dalen, över berget och ner i den andra dalen. Ju högre berget är, desto svårare blir det att ta sig över. Dalarna representerar de två faserna i systemet och när vi tagit oss till den andra dalen, så får vi öar av LFP fasen. Vi har lyckats börja ladda batteriet!

Men det här landskapet är alldeles för simpelt för att beskriva fasomvandlingar i LFP. Det finns andra versioner av den här fjällkedjan, där berget nu istället är uppdelat i två toppar med en liten dal emellan. Den här dalen representerar löslighetsfasen och när man inkluderar en sådan beskrivning i fasfältsmodellen ser situationen väldigt annorlunda ut. Tänk att vi nu laddar ur ett batteri och Li börjar lämna LFP elektroden. Vi tar oss upp för den första toppen, vilar oss i dalen, tar oss upp för den andra och avslutar vår vandring.

I det här fallet så genomgår systemet två fasförändringar under urladdningen av elektroden, först bildas en löslighetsfas och sen en FP fas.

Mina beräkningar visar att när detta förlopp sker snabbt så bildas ett system där alla tre faser finns samtidigt där bilden av partikeln under urladdningen av ett batteri kan liknas vid en smörgås med bröd, smör och pålägg. Löslighetsfasen (smöret då) rör sig mellan LFP och FP fasen vilket gör att urladdningen går snabbare och töjningen mindre. Det i sin tur kan förbättra batteriets livslängd.

Det finns dessutom andra sätt att påverka ordningen av atomer på gittret. Tänk nu tillbaka till fallet med olja och vatten. När man häller lite såpa i så lyckas man få en enheltlig blanding, och vi får en vätska som liknar den med karamellfärg. På samma sätt, så kan man tillsätta små mängder av det kemiska ämnet mangan i LFP materialet och också få en löslighetsfas i systemet som till och med dyker upp i rumstemperatur. Detta gör också att energilandskapet förändras och bergstopparna blir troligtvis lättare att ta sig över. Att kunna förändra hur atomerna ordnar sig i ett gitter kan därför leda till många intressanta egenskaper hos material.

References

[1] J Kennedy, B Trewin, R Betts, P Thorne, and P Foster. State of the Climate 2024. Update for COP29. 2024.

[2] Christoph R. Birkl, Matthew R. Roberts, Euan McTurk, Peter G. Bruce, and David A. Howey. Degradation diagnostics for lithium ion cells. *Journal of Power Sources*, 341:373–386, 2 2017.

[3] Patrick J. Phillips, Javier Bareño, Yan Li, Daniel P. Abraham, and Robert F. Klie. On the Localized Nature of the Structural Transformations of Li_2MnO_3 Following Electrochemical Cycling. *Advanced Energy Materials*, 5(23), 12 2015.

[4] Alice J. Merryweather, Quentin Jacquet, Steffen P. Emge, Christoph Schnedermann, Akshay Rao, and Clare P. Grey. Operando monitoring of single-particle kinetic state-of-charge heterogeneities and cracking in high-rate Li-ion anodes. *Nature Materials*, 21(11):1306–1313, 11 2022.

[5] Guoying Chen, Xiangyun Song, and Thomas J. Richardson. Electron microscopy study of the $LiFePO_4$ to $FePO_4$ phase transition. *Electrochemical and Solid-State Letters*, 9(6):A295, 6 2006.

[6] Hao Liu, Fiona C. Strobridge, Olaf J. Borkiewicz, Kamila M. Wiaderek, Karena W. Chapman, Peter J. Chupas, and Clare P. Grey. Capturing metastable structures during high-rate cycling of $LiFePO_4$ nanoparticle electrodes. *Science*, 344(6191), 6 2014.

[7] Junjie Niu, Akihiro Kushima, Xiaofeng Qian, Liang Qi, Kai Xiang, Yet-Ming Chiang, and Ju Li. In Situ Observation of Random Solid Solution Zone in $LiFePO_4$ Electrode. *Nano Letters*, 14(7):4005–4010, 7 2014.

[8] Christian Masquelier and Laurence Croguennec. Polyanionic (Phosphates, Silicates, Sulfates) Frameworks as Electrode Materials for Rechargeable Li (or Na) Batteries. *Chemical Reviews*, 113(8):6552–6591, 8 2013.

[9] A. Manthiram and J.B. Goodenough. Lithium insertion into Fe2(MO4)3 frameworks: Comparison of M = W with M = Mo. *Journal of Solid State Chemistry*, 71(2):349–360, 12 1987.

[10] A. Manthiram and J.B. Goodenough. Lithium insertion into $Fe_2(SO_4)_3$ frameworks. *Journal of Power Sources*, 26(3-4):403–408, 5 1989.

[11] A. K. Padhi, K. S. Nanjundaswamy, and J. B. Goodenough. Phospho-olivines as Positive-Electrode Materials for Rechargeable Lithium Batteries. *Journal of The Electrochemical Society*, 144(4):1188–1194, 4 1997.

[12] N. Ravet, Y. Chouinard, J.F. Magnan, S. Besner, M. Gauthier, and M. Armand. Electroactivity of natural and synthetic triphylite. *Journal of Power Sources*, 97-98:503–507, 7 2001.

[13] Shyam S. Sharma and Arumugam Manthiram. Towards more environmentally and socially responsible batteries. *Energy & Environmental Science*, 13(11):4087–4097, 2020.

[14] Atsuo Yamada, Hiroshi Koizumi, Noriyuki Sonoyama, and Ryoji Kanno. Phase change in Li_xFePO_4. *Electrochemical and Solid-State Letters*, 8(8):A409, 6 2005.

[15] J. L. Dodd, R. Yazami, and B. Fultz. Phase diagram of Li_xFePO_4. *Electrochemical and Solid-State Letters*, 9(3):A151, 1 2006.

[16] Charles Delacourt, Philippe Poizot, Jean-Marie Tarascon, and Christian Masquelier. The existence of a temperature-driven solid solution in Li_xFePO_4 for $0 \leq x \leq 1$. *Nature Materials*, 4(3):254–260, 3 2005.

[17] Charles Delacourt, Juan Rodríguez-Carvajal, Bernd Schmitt, Jean Marie Tarascon, and Christian Masquelier. Crystal chemistry of the olivine-type Li_xFePO_4 system ($0 \leq x \leq 1$) between 25 and 370 °C. *Solid State Sciences*, 7(12):1506–1516, 12 2005.

[18] K. Zaghib, A. Mauger, J. B. Goodenough, F. Gendron, and C. M. Julien. Electronic, optical, and magnetic properties of $LiFePO_4$: Small magnetic polaron effects. *Chemistry of Materials*, 19(15):3740–3747, 7 2007.

[19] Brian Ellis, Laura K. Perry, Dominic H. Ryan, and L. F. Nazar. Small polaron hopping in Li_xFePO_4 solid solutions: Coupled lithium-ion and electron mobility. *Journal of the American Chemical Society*, 128(35):11416–11422, 9 2006.

[20] Thomas Maxisch, Fei Zhou, and Gerbrand Ceder. Ab initio study of the migration of small polarons in olivine Li_xFePO_4 and their association with lithium ions and vacancies. *Physical Review B*, 73(10):104301, 3 2006.

[21] Jordi Cabana, Junichi Shirakawa, Guoying Chen, Thomas J. Richardson, and Clare P. Grey. MAS NMR study of the metastable solid solutions found in the $LiFePO_4/FePO_4$ system. *Chemistry of Materials*, 22(3):1249–1262, 2 2010.

[22] Fei Zhou, Thomas Maxisch, and Gerbrand Ceder. Configurational electronic entropy and the phase diagram of mixed-valence oxides: The case of Li_xFePO_4. *Physical Review Letters*, 97(15):155704, 10 2006.

[23] Rahul Malik, Aziz Abdellahi, and Gerbrand Ceder. A Critical Review of the Li Insertion Mechanisms in $LiFePO_4$ Electrodes. *Journal of The Electrochemical Society*, 160(5):A3179–A3197, 2013.

[24] Gogi K. Singh, Gerbrand Ceder, and Martin Z. Bazant. Intercalation dynamics in rechargeable battery materials: General theory and phase-transformation waves in LiFePO4. *Electrochimica Acta*, 53(26):7599–7613, 11 2008.

[25] Peng Bai, Daniel A Cogswell, and Martin Z Bazant. Suppression of Phase Separation in $LiFePO_4$ Nanoparticles During Battery Discharge. *Nano Lett*, 11:22, 2011.

[26] Liang Hong, Linsen Li, Yuchen Karen Chen-Wiegart, Jiajun Wang, Kai Xiang, Liyang Gan, Wenjie Li, Fei Meng, Fan Wang, Jun Wang, Yet Ming Chiang, Song Jin, and Ming Tang. Two-dimensional lithium diffusion behavior and probable hybrid phase transformation kinetics in olivine lithium iron phosphate. *Nature Communications 2017 8:1*, 8(1):1–13, 10 2017.

[27] Kaiqi Yang and Ming Tang. Three-dimensional phase evolution and stress-induced non-uniform Li intercalation behavior in lithium iron phosphate. *Journal of Materials Chemistry A*, 8(6):3060–3070, 2 2020.

[28] Alexandros Vasileiadis, Niek J.J. de Klerk, Raymond B. Smith, Swapna Ganapathy, Peter Paul R.M.L. Harks, Martin Z. Bazant, and Marnix

Wagemaker. Toward Optimal Performance and In-Depth Understanding of Spinel $Li_4Ti_5O_{12}$ Electrodes through Phase Field Modeling. *Advanced Functional Materials*, 28(16):1705992, 4 2018.

[29] Peng Bai and Martin Z. Bazant. Charge transfer kinetics at the solid solid interface in porous electrodes. *Nature Communications 2014 5:1*, 5(1):1–7, 4 2014.

[30] Rahul Malik, Fei Zhou, and G. Ceder. Kinetics of non-equilibrium lithium incorporation in $LiFePO_4$. *Nature Materials*, 10(8):587–590, 8 2011.

[31] Nele Moelans, Bart Blanpain, and Patrick Wollants. An introduction to phase-field modeling of microstructure evolution. *Calphad: Computer Coupling of Phase Diagrams and Thermochemistry*, 32(2):268–294, 6 2008.

[32] Mathis Plapp. Phase-Field Models. *Handbook of Crystal Growth: Second Edition*, 1:631–668, 1 2015.

[33] Nikolas Provatas and Ken Elder. *Phase-Field Methods in Materials Science and Engineering*. Wiley-VCH, 10 2010.

[34] Zhiqiang Bi and Robert F. Sekerka. Phase-field model of solidification of a binary alloy. *Physica A: Statistical Mechanics and its Applications*, 261(1-2):95–106, 12 1998.

[35] Wenhao Wu, Ying Lin, Yonggang Hu, Zhifeng He, and Yong Yang. Phase-field modelling for degradation/failure research in lithium battery: Progress and prospects. *Journal of Energy Chemistry*, 11 2024.

[36] Xingxing Jiao, Xuyang Wang, Xieyu Xu, Yongjing Wang, Hoon Hee Ryu, Jimin Park, Jang Yeon Hwang, Shizhao Xiong, YangKook Sun, Zhongxiao Song, and Yangyang Liu. Multi Physical Field Simulation: A Powerful Tool for Accelerating Exploration of High Energy Density Rechargeable Lithium Batteries. *Advanced Energy Materials*, 13(39), 10 2023.

[37] Hill Terrell L. *An introduction to statistical thermodynamics*. Dover Publications, Inc., USA, 1960.

[38] Frenkel Daan and Smit Berend. *Understanding molecular simulation from algorithms to applications*. Academic press, USA, 2002.

[39] Godréche Claude, editor. *Solids far from equilibrium*. Cambridge University Press, USA, 1992.

[40] Anton Van Der Ven, Jishnu Bhattacharya, and Anna A Belak. Understanding Li Diffusion in Li-Intercalation Compounds. *Accounts of Chemical Research*, 46, 2013.

[41] John W. Cahn. On spinodal decomposition. *Acta Metallurgica*, 9(9):795–801, 9 1961.

[42] Anh Thu Phan, Aïmen E. Gheribi, and Patrice Chartrand. Modelling of phase equilibria of $LiFePO_4$-$FePO_4$ olivine join for cathode material. *The Canadian Journal of Chemical Engineering*, 97(8):2224–2233, 8 2019.

[43] Hans Lukas, Suzana G. Fries, and Bo Sundman. *Computational Thermodynamics: The Calphad Method*. Cambridge University Press, USA, 1st edition, 2007.

[44] A. Van der Ven, K. Garikipati, S. Kim, and M. Wagemaker. The Role of Coherency Strains on Phase Stability in Li_xFePO_4: Needle Crystallites Minimize Coherency Strain and Overpotential. *Journal of The Electrochemical Society*, 156(11):A949, 2009.

[45] J. Lund, H. Wang, R. D. Braatz, and R. E. García. Machine learning of phase diagrams. *Materials Advances*, 3(23):8485–8497, 2022.
[46] Daniel A. Cogswell and Martin Z. Bazant. Coherency strain and the kinetics of phase separation in $LiFePO_4$ nanoparticles. *ACS Nano*, 6(3):2215–2225, 3 2012.
[47] Simon Daubner, Marcel Weichel, Daniel Schneider, and Britta Nestler. Modeling intercalation in cathode materials with phase-field methods: Assumptions and implications using the example of $LiFePO_4$. *Electrochimica Acta*, 421:140516, 7 2022.
[48] Michael J. Welland, Dmitry Karpeyev, Devin T. O'Connor, and Olle Heinonen. Miscibility Gap Closure, Interface Morphology, and Phase Microstructure of 3D Li_xFePO_4 Nanoparticles from Surface Wetting and Coherency Strain. *ACS Nano*, 9(10):9757–9771, 10 2015.
[49] Ming Tang, James F. Belak, and Milo R. Dorr. Anisotropic phase boundary morphology in nanoscale olivine electrode particles. *Journal of Physical Chemistry C*, 115(11):4922–4926, 3 2011.
[50] S. Bulent Biner. *Programming Phase-Field Modeling*. Springer International Publishing, Cham, 2017.
[51] Martin Z. Bazant. Unified quantum theory of electrochemical kinetics by coupled ion–electron transfer. *Faraday Discussions*, 246:60–124, 2023.
[52] Christopher E. D. Chidsey. Free Energy and Temperature Dependence of Electron Transfer at the Metal-Electrolyte Interface. *Science*, 251(4996):919–922, 2 1991.
[53] David T. Boyle, Xian Kong, Allen Pei, Paul E. Rudnicki, Feifei Shi, William Huang, Zhenan Bao, Jian Qin, and Yi Cui. Transient Voltammetry with Ultramicroelectrodes Reveals the Electron Transfer Kinetics of Lithium Metal Anodes. *ACS Energy Letters*, 5(3):701–709, 3 2020.
[54] Daniel A. Cogswell. Quantitative phase-field modeling of dendritic electrodeposition. *Physical Review E*, 92(1):011301, 7 2015.
[55] Joakim Halldin Stenlid, Pjotrs Žguns, Daniele Vivona, Abhishek Aggarwal, Kiarash Gordiz, Yirui Zhang, Shakul Pathak, Martin Z. Bazant, Yang Shao-Horn, Artem Baskin, and John W. Lawson. Computational Insights into Electrolyte-Dependent Li-Ion Charge-Transfer Kinetics at the Li_xCoO_2 Interface. *ACS Energy Letters*, 9(7):3608–3617, 7 2024.
[56] Yirui Zhang, Dimitrios Fraggedakis, Tao Gao, Shakul Pathak, Debbie Zhuang, Cristina Grosu, Yash Samantaray, Armando R.C. Neto, Sravani R. Duggirala, Botao Huang, Yun Guang Zhu, Livia Giordano, Ryoichi Tatara, Harsh Agarwal, Ryan M. Stephens, Martin Z. Bazant, and Yang Shao-Horn. Lithium-ion intercalation by coupled ion-electron transfer, 5 2024.
[57] Yi Zeng, Raymond B. Smith, Peng Bai, and Martin Z. Bazant. Simple formula for Marcus Hush Chidsey kinetics. *Journal of Electroanalytical Chemistry*, 735:77–83, 12 2014.
[58] Anders Logg, Kent-Andre Mardal, and Garth Wells, editors. *Automated Solution of Differential Equations by the Finite Element Method*, volume 84 of *Lecture Notes in Computational Science and Engineering*. Springer Berlin Heidelberg, Berlin, Heidelberg, 2012.
[59] Martin S Alnaes, Jan Blechta, Johan Hake, August Johansson, Benjamin Kehlet,

Anders Logg, Chris Richardson, Johannes Ring, Marie E Rognes, and Garth N Wells. The FEniCS Project Version 1.5. *Archive of Numerical Software*, 3(100), 12 2015.

[60] Akshay Krishna Akshay, Eddie Wadbro, Christof Köhler, Pavlin Mitev, Peter Broqvist, and Jolla Kullgren. CCS: A software framework to generate two-body potentials using Curvature Constrained Splines. *Computer Physics Communications*, 258:107602, 1 2021.

[61] Mattias ngqvist, William A. Muoz, J. Magnus Rahm, Erik Fransson, Cline Durniak, Piotr Rozyczko, Thomas H. Rod, and Paul Erhart. ICET - A Python Library for Constructing and Sampling Alloy Cluster Expansions. *Advanced Theory and Simulations*, 2(7), 7 2019.

[62] A. Fernández-Caballero, J. S. Wróbel, P. M. Mummery, and D. Nguyen-Manh. Short-Range Order in High Entropy Alloys: Theoretical Formulation and Application to Mo-Nb-Ta-V-W System. *Journal of Phase Equilibria and Diffusion*, 38(4):391–403, 8 2017.

[63] J.M. Sanchez, F. Ducastelle, and D. Gratias. Generalized cluster description of multicomponent systems. *Physica A: Statistical Mechanics and its Applications*, 128(1-2):334–350, 11 1984.

[64] Luis Barroso-Luque, Peichen Zhong, Julia H. Yang, Fengyu Xie, Tina Chen, Bin Ouyang, and Gerbrand Ceder. Cluster expansions of multicomponent ionic materials: Formalism and methodology. *Physical Review B*, 106(14):144202, 10 2022.

[65] Wolfram Koch and Max C. Holthausen. *A Chemist's Guide to Density Functional Theory*. Wiley, 7 2001.

[66] P. Hohenberg and W. Kohn. Inhomogeneous electron gas. *Physical Review*, 136(3B):B864, 11 1964.

[67] Narbe Mardirossian and Martin Head-Gordon. Thirty years of density functional theory in computational chemistry: an overview and extensive assessment of 200 density functionals. *Molecular Physics*, 115(19):2315–2372, 10 2017.

[68] John P. Perdew, Kieron Burke, and Matthias Ernzerhof. Generalized Gradient Approximation Made Simple. *Physical Review Letters*, 77(18):3865, 10 1996.

[69] G. Kresse and J. Furthmüller. Efficient iterative schemes for ab initio total-energy calculations using a plane-wave basis set. *Physical Review B*, 54(16):11169, 10 1996.

[70] G. Kresse and J. Furthmüller. Efficiency of ab-initio total energy calculations for metals and semiconductors using a plane-wave basis set. *Computational Materials Science*, 6(1):15–50, 7 1996.

[71] Jeremy P. Allen and Graeme W. Watson. Occupation matrix control of d- and f-electron localisations using DFT + U. *Physical Chemistry Chemical Physics*, 16(39):21016–21031, 9 2014.

[72] Nongluk Meethong, Hsiao Ying Shadow Huang, Scott A. Speakman, W. Craig Carter, and Yet Ming Chiang. Strain Accommodation during Phase Transformations in Olivine-Based Cathodes as a Materials Selection Criterion for High-Power Rechargeable Batteries. *Advanced Functional Materials*, 17(7):1115–1123, 5 2007.

[73] Boris Dorado, Bernard Amadon, Michel Freyss, and Marjorie Bertolus. DFT+U

calculations of the ground state and metastable states of uranium dioxide. *Physical Review B*, 79(23):235125, 6 2009.

[74] Patrick H.L. Sit, Roberto Car, Morrel H. Cohen, and Annabella Selloni. Simple, unambiguous theoretical approach to oxidation state determination via first-principles calculations. *Inorganic Chemistry*, 50(20):10259–10267, 10 2011.

[75] Amalie Skurtveit, Erlend Tiberg North, Heesoo Park, Dmitry Chernyshov, David S. Wragg, and Alexey Y. Koposov. Stepwise Structural Relaxation in Battery Active Materials. *ACS Materials Letters*, 17:343–349, 1 2024.

[76] Yujie Zhu, Jiang Wei Wang, Yang Liu, Xiaohua Liu, Akihiro Kushima, Yihang Liu, Yunhua Xu, Scott X Mao, Ju Li, Chunsheng Wang, Jian Yu Huang, Y Zhu, Y Liu, Y Xu, C Wang, J W Wang, S X Mao, X Liu, J Y Huang, A Kushima, and J Li. In Situ Atomic-Scale Imaging of Phase Boundary Migration in $FePO_4$ Microparticles During Electrochemical Lithiation. *Advanced Materials*, 25(38):5461–5466, 10 2013.

[77] Neeraj Sharma, Xianwei Guo, Guodong Du, Zaiping Guo, Jiazhou Wang, Zhaoxiang Wang, and Vanessa K. Peterson. Direct evidence of concurrent solid-solution and two-phase reactions and the nonequilibrium structural evolution of $LiFePO_4$. *Journal of the American Chemical Society*, 134(18):7867–7873, 5 2012.

[78] Young-Sang Yu, Maryam Farmand, Chunjoong Kim, Yijin Liu, Clare P. Grey, Fiona C. Strobridge, Tolek Tyliszczak, Rich Celestre, Peter Denes, John Joseph, Harinarayan Krishnan, Filipe R. N. C. Maia, A. L. David Kilcoyne, Stefano Marchesini, Talita Perciano Costa Leite, Tony Warwick, Howard Padmore, Jordi Cabana, and David A. Shapiro. Three-dimensional localization of nanoscale battery reactions using soft X-ray tomography. *Nature Communications*, 9(1):921, 3 2018.

[79] D. B. Ravnsbæk, K. Xiang, W. Xing, O. J. Borkiewicz, K. M. Wiaderek, P. Gionet, K. W. Chapman, P. J. Chupas, and Y. M. Chiang. Extended solid solutions and coherent transformations in nanoscale olivine cathodes. *Nano Letters*, 14(3):1484–1491, 3 2014.

[80] Tatsuya Nakamura, Yoshiki Miwa, Mitsuharu Tabuchi, and Yoshihiro Yamada. Structural and Surface Modifications of $LiFePO_4$ Olivine Particles and Their Electrochemical Properties. *Journal of The Electrochemical Society*, 153(6):A1108, 2006.

[81] Tatsuya Nakamura, Kiyotaka Sakumoto, Shiro Seki, Yo Kobayashi, Mitsuharu Tabuchi, and Yoshihiro Yamada. Apparent Diffusion Constant and Electrochemical Reaction in $LiFe_{1x}Mn_xPO_4$ Olivine Cathodes. *Journal of The Electrochemical Society*, 154(12):A1118, 2007.

[82] Kyung Tae Lee and Kyung Sub Lee. Electrochemical properties of $LiFe_{0.9}Mn_{0.1}PO_4/Fe_2P$ cathode material by mechanical alloying. *Journal of Power Sources*, 189(1):435–439, 4 2009.

[83] Rahul Malik, Fei Zhou, and Gerbrand Ceder. Phase diagram and electrochemical properties of mixed olivines from first-principles calculations. *Physical Review B*, 79(21):214201, 6 2009.

[84] Yuan Liu, Yi Jing Gu, Jia Li Deng, Gui Yang Luo, Fu Zhong Wu, Yi Mai, Xin Yi Dai, and Jun Qi Li. Effect of doped Mn on improving the

electrochemical performance of $LiFePO_4$. *Journal of Materials Science: Materials in Electronics*, 31(4):2887–2894, 2 2020.

[85] Yan Wang, Zhe Sheng Feng, Lu Lin Wang, Le Yu, Jin Ju Chen, Zi Liang, and Rui Wang. A joint experimental and theoretical study on the effect of manganese doping on the structural, electrochemical and physical properties of lithium iron phosphate. *RSC Advances*, 4(93):51609–51614, 10 2014.

[86] Gerard Bree, Jingyi Zhao, Veronika Majherova, Daniela Proprentner, Galo J. Paez Fajardo, and Louis F. J. Piper. Practical Pathways to Higher Energy Density LMFP Battery Cathodes. *Energy & Fuels*, 2 2025.

[87] Atsuo Yamada, Yuki Takei, Hiroshi Koizumi, Noriyuki Sonoyama, Ryoji Kanno, Keiji Itoh, Masao Yonemura, and Takashi Kamiyama. Electrochemical, magnetic, and structural investigation of the $Li_x(Mn_yFe_{1-y})PO_4$ olivine phases. *Chemistry of Materials*, 18(3):804–813, 2 2006.

[88] Ananya Renuka Balakrishna, Yet-Ming Chiang, and W. Craig Carter. Phase-field model for diffusion-induced grain boundary migration: An application to battery electrodes. *Physical Review Materials*, 3(6):065404, 6 2019.

[89] Shu Zhang, Zhuo Yang, Yong Lu, Weiwei Xie, Zhenhua Yan, and Jun Chen. Insights into Cation Migration and Intermixing in Advanced Cathode Materials for Lithium-Ion Batteries. *Advanced Energy Materials*, 6 2024.

Acta Universitatis Upsaliensis

Digital Comprehensive Summaries of Uppsala Dissertations from the Faculty of Science and Technology 2505

Editor: The Dean of the Faculty of Science and Technology

A doctoral dissertation from the Faculty of Science and Technology, Uppsala University, is usually a summary of a number of papers. A few copies of the complete dissertation are kept at major Swedish research libraries, while the summary alone is distributed internationally through the series Digital Comprehensive Summaries of Uppsala Dissertations from the Faculty of Science and Technology. (Prior to January, 2005, the series was published under the title "Comprehensive Summaries of Uppsala Dissertations from the Faculty of Science and Technology".)

Distribution: publications.uu.se
urn:nbn:se:uu:diva-550510

ACTA UNIVERSITATIS
UPSALIENSIS
2025